Click Here for Full Article

Submeter bathymetric mapping of volcanic and hydrothermal features on the East Pacific Rise crest at 9°50′N

Vicki Lynn Ferrini
Applied Ocean Physics and Engineering Department, Deep Submergence Laboratory, Woods Hole Oceanographic Institution, Woods Hole, Massachusetts 02543, USA (vferrini@whoi.edu)

Daniel J. Fornari
Marine Geology and Geophysics Department, Woods Hole Oceanographic Institution, Woods Hole, Massachusetts 02543, USA

Timothy M. Shank
Biology Department, Woods Hole Oceanographic Institution, Woods Hole, Massachusetts 02543, USA

James C. Kinsey
Department of Mechanical Engineering, Johns Hopkins University, Baltimore, Maryland 21218, USA

Maurice A. Tivey and S. Adam Soule
Marine Geology and Geophysics Department, Woods Hole Oceanographic Institution, Woods Hole, Massachusetts 02543, USA

Suzanne M. Carbotte
Lamont–Doherty Earth Observatory of Columbia University, Palisades, New York 10964, USA

Louis L. Whitcomb
Applied Ocean Physics and Engineering Department, Deep Submergence Laboratory, Woods Hole Oceanographic Institution, Woods Hole, Massachusetts 02543, USA

Department of Mechanical Engineering, Johns Hopkins University, Baltimore, Maryland 21218, USA

Dana Yoerger and Jonathan Howland
Applied Ocean Physics and Engineering Department, Deep Submergence Laboratory, Woods Hole Oceanographic Institution, Woods Hole, Massachusetts 02543, USA

[1] Recent advances in underwater vehicle navigation and sonar technology now permit detailed mapping of complex seafloor bathymetry found at mid-ocean ridge crests. Imagenex 881 (675 kHz) scanning sonar data collected during low-altitude (∼5 m) surveys conducted with DSV *Alvin* were used to produce submeter resolution bathymetric maps of five hydrothermal vent areas at the East Pacific Rise (EPR) Ridge2000 Integrated Study Site (9°50′N, "bull's-eye"). Data were collected during 29 dives in 2004 and 2005 and were merged through a grid rectification technique to create high-resolution (0.5 m grid) composite maps. These are the first submeter bathymetric maps generated with a scanning sonar mounted on *Alvin*. The composite maps can be used to quantify the dimensions of meter-scale volcanic and hydrothermal features within the EPR axial summit trough (AST) including hydrothermal vent structures, lava pillars, collapse areas, the trough walls, and primary volcanic fissures. Existing Autonomous Benthic Explorer (ABE) bathymetry data (675 kHz scanning sonar) collected at this site provide the broader

geologic context necessary to interpret the meter-scale features resolved in the composite maps. The grid rectification technique we employed can be used to optimize vehicle time by permitting the creation of high-resolution bathymetry maps from data collected during multiple, coordinated, short-duration surveys after primary dive objectives are met. This method can also be used to colocate future near-bottom sonar data sets within the high-resolution composite maps, enabling quantification of bathymetric changes associated with active volcanic, hydrothermal and tectonic processes.

1. Introduction

[2] Bathymetric mapping of deep-water environments is often conducted with oceanographic research vessels equipped with ship-mounted multibeam systems. The resolution of these systems is limited by ship motion, relatively low acoustic frequency (~12 kHz), long acoustic ranges, water column sound velocity variability, and finite beam angles. As a result, the vertical and horizontal resolution of bathymetric maps generated with ship-mounted multibeam systems are on the order of several tens to several hundreds of meters, respectively [e.g., *de Moustier*, 1988]. Near-bottom high-resolution (<5 m horizontal and vertical scale) bathymetric data are required to investigate the complex seabed morphology created by volcanic and tectonic processes and hydrothermal venting at mid-ocean ridges (MORs) [e.g., *Chadwick et al.*, 2001; *Shank et al.*, 2003; *Cormier et al.*, 2003; *Fornari et al.*, 2004; *Yoerger et al.*, 1996; *Embley*, 2002; *Jakuba et al.*, 2002; *Roman et al.*, 2005]. With data of this resolution, the distribution and volcanic/structural context of high- and low-temperature hydrothermal venting along MOR crest can be deduced and used to correlate and study the linkages between hydrothermal, biological, geological, and geophysical processes within the context of the surrounding seafloor terrain.

[3] High-resolution mapping efforts in deep-water environments are frequently conducted with deeply towed vehicle platforms [e.g., *Haymon et al.*, 1991; *Bachmayer et al.*, 1998; *Fornari et al.*, 1998a, 2004; *Sinton et al.*, 2002; *Schouten et al.*, 2002;

Hey et al., 2004; D. J. Fornari et al., AHA-Nemo2 Cruise Report cruise data Web site, http://science. whoi.edu/ahanemo2, 2001]. The DSL-120A system, for example, is a deep-towed vehicle employing a 120 kHz phase bathymetric side-scan sonar with side-scan swath width of 1000 m, typical phase bathymetric swath width of 400 m, and bathymetry resolution on the order of 2−4 m [*Scheirer et al.*, 2000]. Recent technological advances have also enabled precision deep-water surveys with both remotely operated vehicles (ROVs) [*Ballard et al.*, 2000; *Whitcomb et al.*, 2000; *Singh et al.*, 2000] and Autonomous Underwater Vehicles (AUVs) [e.g., *Yoerger et al.*, 1996; *Schouten et al.*, 2002; *Shank et al.*, 2003]. The Jason 2 Remote Operated Vehicle (ROV) system, for example, is frequently equipped with 675 kHz scanning pencil beam sonar and a 200 kHz multibeam sonar for near-bottom bathymetric surveys, both with vertical resolution as high as centimeters to decimeters depending on acquisition parameters [*Singh et al.*, 2000; *Whitcomb et al.*, 2000; *Roman et al.*, 2005; *Ferrini et al.*, 2005b]. Similarly, the submersible *Alvin* is routinely equipped with a 675 kHz scanning sonar system to generate high-resolution seafloor maps [e.g., *Kurras et al.*, 1998; *Chadwick et al.*, 2001; *Soule et al.*, 2005].

[4] The increased resolution obtained with near-bottom surveys conducted with any deep submergence platform requires increased survey time because the swath width of multibeam and scanning pencil beam sonar systems is fundamentally limited by vehicle altitude. The efficiency with which mapping goals can be achieved, however,
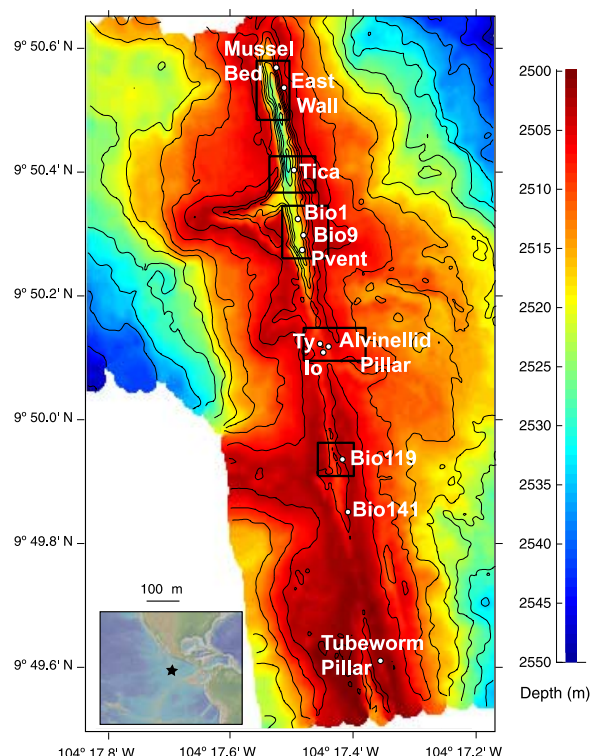
Figure 1a. East Pacific Rise, Ridge2000 integrated study site (ISS) near 9°50′N showing vent locations on 5-m gridded bathymetry (5-m contours) based on ABE surveys [*Fornari et al.*, 2004]. The locations of the five composite maps shown in the following figures are outlined in black and were generated using data from multiple *Alvin* dives. Inset shows location of EPR study area.

can be greatly increased by using data from short-duration, coordinated surveys during one or more cruises to the same area to create composite bathymetric maps.

[5] Combining spatial data collected during multiple dives of deep submergence vehicles is complicated by underwater vehicle navigation limitations. Vehicles with precise underwater vehicle navigational systems can log horizontal errors of up to 10 m during a single dive [*Whitcomb et al.*, 1998, 1999a, 1999b; *Kinsey and Whitcomb*, 2004]. Larger offsets are not atypical between multiple dives performed within the same acoustic navigation network. The bathymetric complexity of MOR crests, where vertical changes can be as large as 10 m over horizontal distances of a few meters, may induce significant errors in high-resolution maps if navigational data are inaccurate. Using

seafloor features as natural benchmarks to merge data from multiple dives provides a means for overcoming navigational limitations and for quantifying and correcting navigational offsets associated with vehicle positioning strategies.

[6] The Ridge2000 program aims to study the linkages between hydrothermal, biological, geological and geophysical processes within sites of focused investigation on the East Pacific Rise, Juan de Fuca Ridge, and in the Lau Basin (http://www.ridge2000.org/). Repeat near-bottom programs with *Alvin* and *Jason 2* are a key component of ongoing work at these sites and provide the opportunity to collect high-resolution bathymetry as a low-impact add-on to existing programs undertaken for biological and hydrothermal sampling goals.

[7] In this paper, we present high-resolution (submeter) composite maps created through the development of a grid rectification technique that combines tide-corrected, high-frequency (675 kHz) Imagenex scanning altimetric sonar data collected during multiple *Alvin* submersible dives at the EPR near 9°50′N (Figures 1a and 1b). We present five small composite maps (0.5 m grid) (areas ranging from 1100 m^2 and 2100 m^2) focused around many of the well-studied active hydrothermal vent structures at this site as well as a 2 m × 5 m gridded map of previously reported Autonomous Benthic Explorer (ABE) data collected within the axial summit trough (AST) from 9°49.6′N to 9°50.6′N [*Yoerger et al.*, 1996; *Schouten et al.*, 2002; *Fornari et al.*, 2004; *Soule et al.*, 2005; J. Escartin et al., Interactions between faults and lava flows along the East Pacific Rise crest (9°10′–50′N): Implications for upper oceanic crust construction, submitted to *Geochemistry, Geophysics, Geosystems*, 2006, hereinafter referred to as Escartin et al., submitted manuscript, 2006]. The high-resolution grids reveal bathymetric features associated with individual vent structures, volcanic fissures and collapse features, and provide base maps upon which sample locations can be accurately placed. The composite grids, and the techniques we employ to create them, can be used to optimize data acquisition strategies and submersible bottom time during multidisciplinary cruises with a wide range of dive objectives. Using these techniques, repeat surveys can be performed to assess temporal changes associated with ridge crest processes, including volcanic eruptions, diking, and evolution of hydrothermal systems and biological communities.
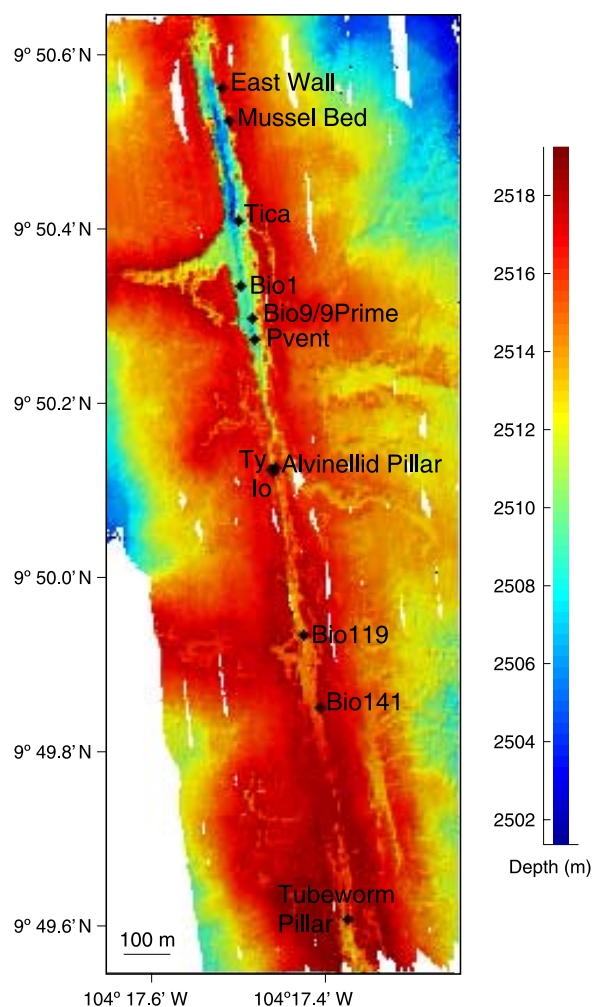
Figure 1b. High-resolution map (2 m east–west × 5 m north–south) generated from previously reported ABE Imagenex sonar data [*Fornari et al.*, 2004]. In this map, more details of the complex AST bathymetry can be discerned. Until now, these data have only been gridded at 5 m × 5 m resolution (see Figure 1a).

1.1. Ridge Crest Setting

[8] The northern EPR in the 9°50′N area has been studied extensively over the past few decades using many geophysical techniques [e.g., *Detrick et al.*, 1987; *Macdonald et al.*, 1984, 1992; *Haymon et al.*, 1991; *Fornari et al.*, 1998a, 2004]. Volcanic and hydrothermal activity at this site is narrowly focused within the ~40- to 100-m-wide AST of the EPR between 9°46′ and 51′N [*Haymon et al.*, 1991, 1993; *Von Damm et al.*, 1996; *Shank et al.*, 1998; *Fornari et al.*, 1998a, 1998b, 2004; *Von Damm*, 2000; *Von Damm and Lilley*, 2004] (Figures 1a and 1b). In March 1991, the first "witnessed" submarine volcanic eruption was observed and preliminarily mapped within the AST between 9°46′ and

51′N, and samples of the hydrothermal fluids and biology were recovered [*Haymon et al.*, 1993; *Rubin et al.*, 1994; *Lutz et al.*, 1994; *Gregg et al.*, 1996; *Shank et al.*, 1998; *Von Damm*, 2000]. High-temperature vents within the floor and along the walls of the AST are primarily located along the trace of the 1991–1992 eruptive volcanic fissures or along fractures above the dike swarm located beneath the AST that tap the vigorous hydrothermal system at the EPR axis [*Haymon et al.*, 1993; *Fornari et al.*, 1998a, 2004; *Shank et al.*, 1998; *Von Damm*, 2000; *Von Damm and Lilley*, 2004]. The hydrothermal systems in this area are believed to be driven by a shallow magma lens at ~1.5 km depth [*Detrick et al.*, 1987; *Kent et al.*, 1994] and focused by vertical to near-vertical dike(s) that sourced the 1991–1992 eruptions and permeable zones created by drain back of magma along the widest portions of the fissure [*Fornari et al.*, 2004].

[9] Three primary environments for high-temperature (hi-T) and low-temperature (low-T) hydrothermal venting have been observed at the EPR 9°50′N area. In the first environment, both high- and low-T venting occurs within and along the trace of the primary eruptive fissure system on the floor of the AST. Tica, Bio9/9prime, P vent, and Tubeworm Pillar are all hi-T areas that occur in this type of environment, while Bio119, Bio141 are low-T diffuse sites also located along the primary fissure system (Figures 1a and 1b). The second venting environment is primarily along the east wall of the AST where both low-T diffuse venting (e.g., East Wall *Riftia* site, Figures 1a and 1b) and high-T focused flow occur (e.g., Alvinellid Pillar, Figures 1a and 1b; M and Q vents (see *Haymon et al.* [1993], *Shank et al.* [1998], *Von Damm* [2000], and *Fornari et al.* [2004] for vent locations). The third area of venting is low-T diffuse flow immediately outside the AST on lobate or sheet lava where extensive collapse is observed (e.g., Mussel Bed, Figures 1a and 1b). The collapsed nature of the volcanic terrain within ~300 m of the AST [*Engels et al.*, 2003; *Fornari et al.*, 1998a, 2004], and the plexus of subseafloor conduits (e.g., lava tubes) provide permeable pathways for diluted hydrothermal fluids to migrate immediately outside the trough [*Haymon et al.*, 1993].

1.2. Previous Mapping at the EPR 9°50′N

[10] Multibeam sonar data at 30–100 m grid resolution have been collected on numerous expeditions to the EPR near 9°50′N during the past two decades [e.g., *Macdonald et al.*, 1984, 1992;

Fornari et al., 1988, 1998a; *Toomey et al.*, 1994; *Dunn and Toomey*, 1997; *Cochran et al.*, 1999; *White et al.*, 2006]. Aside from single, near-bottom altimeter profiles acquired during *Alvin* dives, no fine-scale (<80 m grid resolution), baseline bathymetric maps were available for this area until about 5 years ago. In late 2005, an EM300 survey of the EPR between 12°N and 8°N was carried out during a transit of the R/V *T. Thompson* from San Diego to the Galapagos [*White et al.*, 2006]. Those data provide a fourfold improvement in the multibeam grid cell resolution of the EPR axis and crest over the study area. Near-bottom sonar and precision vehicle navigation technology have only recently permitted highly detailed (~1−5 m resolution) bathymetric surveys to be carried out at this and other MOR sites [e.g., *Kurras et al.*, 2000; *Chadwick et al.*, 2001; *Johnson et al.*, 2002; *Jakuba et al.*, 2002; *Cormier et al.*, 2003; *Kelley et al.*, 2005; *Embley*, 2002; *Yoerger et al.*, 2002; *Fornari et al.*, 2004; *Soule et al.*, 2005].

[11] A narrow (~400 m wide) swath along the EPR axis between ~9°10′N and 9°55′N was mapped in 1989 using a 100 kHz analog-output side-scan sonar mounted on the Argo mapping system [*Haymon et al.*, 1991; *Fornari et al.*, 1998a]. In 2001, a large area of EPR crest over ~5 km across axis and for ~90 km along axis between 9°25′−55′N was imaged using the DSL-120A (120 kHz) digital side scan sonar [*Fornari et al.*, 2004; *Schouten et al.*, 2002; D. J. Fornari et al., AHA-Nemo2 Cruise Report cruise data Web site, http://science. whoi.edu/ahanemo2, 2001; A. Soule et al., manuscript in preparation, 2006] during two cruises (R/V *Melville* AHA-Nemo2 and R/V *Atlantis* AT7-4). Portions of the trough between 9°49.5′N and 9°51′N, and near 9°28′N, were mapped in 2001 using a 675 kHz Imagenex pencil beam altimeter on the autonomous vehicle ABE (nominal altitude ~40 m) resulting in maps with 1 m vertical resolution and ~5 m horizontal resolution [*Yoerger et al.*, 1996; *Schouten et al.*, 2002; *Fornari et al.*, 2004; *Soule et al.*, 2005] (Figures 1a and 1b). These data were used to generate the first comprehensive high-resolution side-scan sonar and bathymetry maps for the EPR, extending for ~2 km along the axis and ~4−5 km across axis in the 9°50′N and 9°29′N areas [*Fornari et al.*, 2004; A. Soule et al., manuscript in preparation, 2006]. Although these data provide large area, fine-scale bathymetric control on the volcanic features (e.g., lava flow fronts, 5−10 m wide, 1−5 m high), they do not have the submeter resolution required to identify and spatially relate hydrothermal and volcano-structural features

(<2 m horizontal resolution), especially within the complex AST.

[12] We present the first submeter resolution grids of EPR axial bathymetry collected with a mechanically scanning altimetric sonar mounted on *Alvin*. The composite maps were generated through further development of previously reported navigation [*Kinsey and Whitcomb*, 2004] and sonar processing routines [*Ballard et al.*, 2000; *Whitcomb et al.*, 2000; *Singh et al.*, 2000], and are nested within the existing ABE bathymetry data collected at 9°50′N [*Yoerger et al.*, 1996; *Schouten et al.*, 2002; *Fornari et al.*, 2004; *Soule et al.*, 2005; Escartin et al., submitted manuscript, 2006; A. Soule et al., manuscript in preparation, 2006]. The data acquisition methods, strategies and processing routines discussed below, provide a framework to quantify the microscale bathymetric character of this fast spreading MOR crest.

2. Data Acquisition

2.1. Navigation

[13] During all dives when Imagenex sonar data were collected, *Alvin* was navigated using a bottom lock Doppler Velocity Log (DVL) sonar (1200 kHz), long-baseline (LBL) navigation [*Hunt et al.*, 1974; *Milne*, 1983], pressure depth sensors, and a north seeking gyrocompass to compute the 3-dimensional location of the vehicle within a geographic frame of reference [*Whitcomb et al.*, 2003; *Kinsey and Whitcomb*, 2004]. DVLNAV software (http:// robotics.me.jhu.edu/dvlnav/) [*Kinsey and Whitcomb*, 2004] was used to integrate the navigational and attitude data strings into an interface that displayed real-time vehicle position in *Alvin*, permitting bathymetric data acquisition along predetermined survey lines.

[14] When combined with LBL navigation, precision depth measurements, and gyrocompass attitude data, DVL navigation can result in vehicle positioning accuracy ranging from submeter to tens of meters depending on deployment geometry and conditions [*Kinsey and Whitcomb*, 2004, 2006]. Navigational errors can, however, be significantly larger due to the combined effects of (1) loss of Doppler bottom lock when the vehicle altitude is either too high or too low; (2) cumulative errors in the Doppler velocity data; (3) errors associated with time-varying alignment of the Doppler and gyro sensors due to the deformation of the vehicle frame caused by changes in weight, ballast, payload, and trim; (4) LBL transponder watch circle
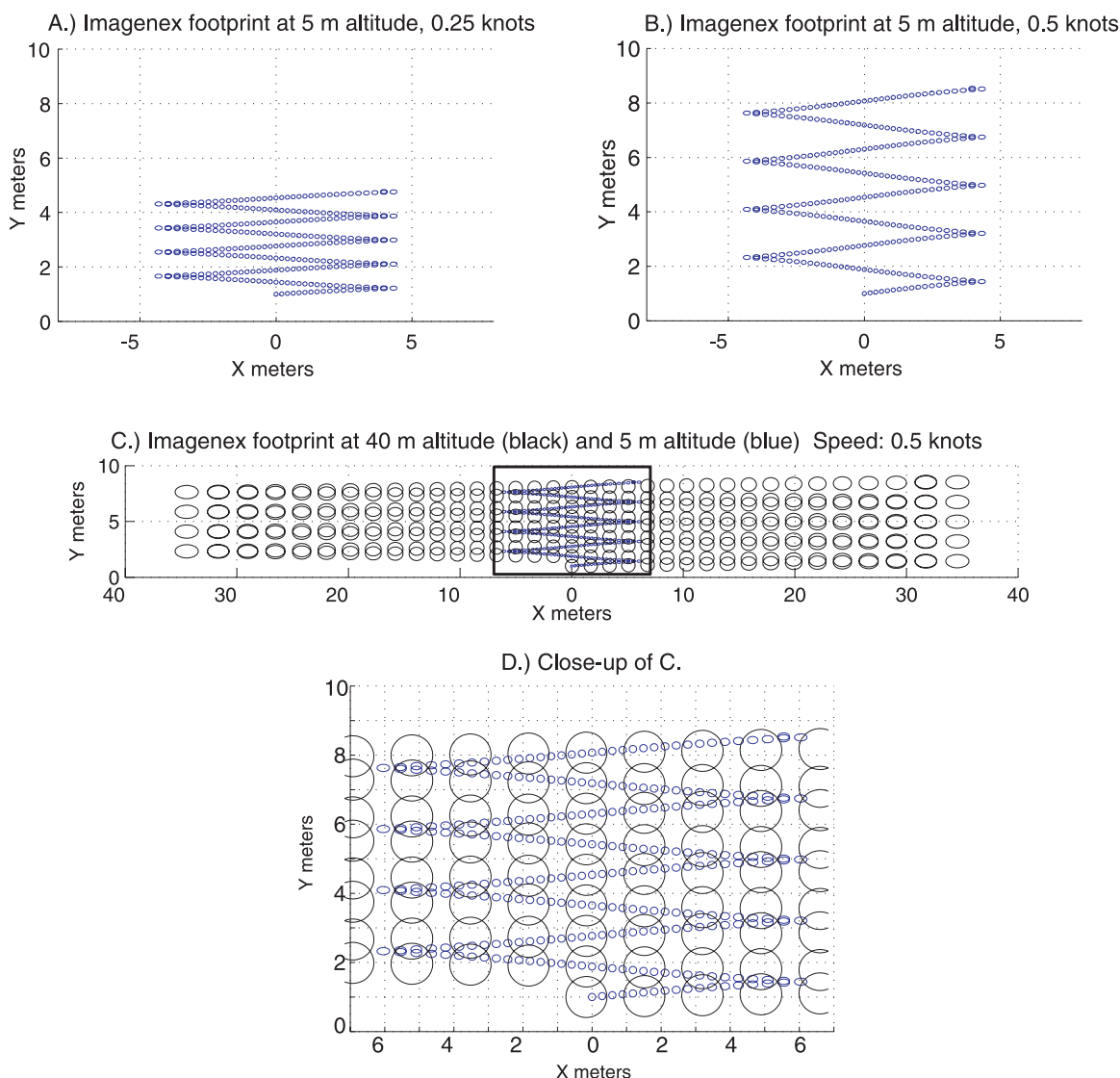
Figure 2. Schematic of Imagenex scanning altimeter footprint at different survey altitudes and speeds assuming a flat seafloor. (a) At an altitude of 5 m, the effective swath width of the scanning sonar is nearly 10 m, and data from subsequent scans are less than 1 m apart in the along-track direction. (b) Increasing survey speed to 0.5 knots (0.25 m/s) does not affect the effective swath width but decreases along-track data density such that subsequent scans are roughly 2 m apart. (c) By increasing the survey altitude to 25 m, the effective swath width is increased to roughly 45 m, and (d) the acoustic footprint is significantly larger. Although increased altitude results in a wider effective swath, the increased footprint size can result in lower-resolution bathymetric maps due to an under-sampling of complex seafloor morphology.

motion; and (5) loss of LBL in high-relief terrain due to acoustic shadowing. Previously reported studies suggest that a poor estimate of the Doppler-Gyro alignment can also result in errors in Doppler navigation [*Whitcomb et al.*, 1999a, 1999b]. *Kinsey and Whitcomb* [2002] provide a methodology for estimating this alignment with submersibles, and the method has also been evaluated on data from a field-deployed AUV [*Kinsey and Whitcomb*, 2006]. For the *Alvin* data used to

generate composite grids in this study, navigational inconsistencies of up to 10 m during a single dive and offsets on the order of tens of meters between multiple dives at a single site were observed.

2.2. Imagenex 881 Scanning Sonar

[15] The Imagenex 881 is a mechanically scanning altimeter with a 1.7° conical beam that sweeps side to side, and, when mounted in down-looking
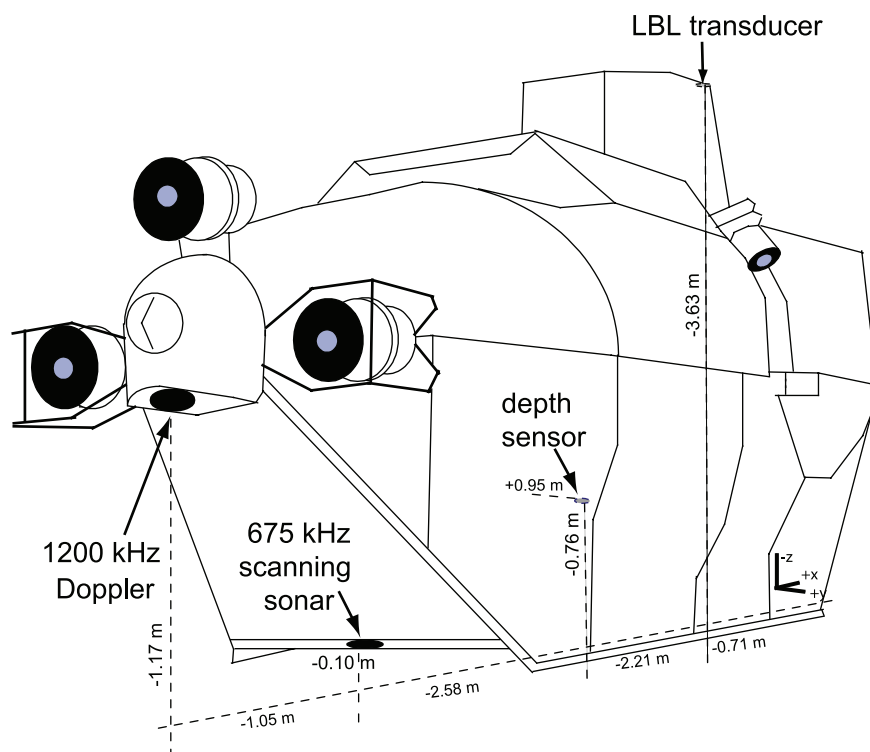
Figure 3. Schematic of *Alvin* indicating offsets between various sensors that collect data necessary to convert sonar returns into geo-referenced bathymetry soundings (see Table 1 for listing of relative offsets). Offsets are with respect to the origin of the vehicle coordinate frame (forward, bottom, center). The X axis is negative in the aft direction, the Y axis is negative toward port, and the Z axis is negative toward the top. With the exception of the paroscientific depth sensor, all sensors are located along the center line in the y direction. Note that the precise locations of these sensors will be different after each vehicle overhaul. (For additional information on *Alvin*, see http://www.whoi.edu/marops/vehicles/alvin/index.html. For additional information on DVL navigation, see http://robotics.me.jhu.edu/dvlnav/.)

mode, results in a slalom of bathymetric soundings along the seafloor as the vehicle advances (Figure 2). The effective swath width is user-defined and can be set from 0° to 180°. The acoustic footprint, which increases with distance to target, is smaller and more circular near nadir, and elliptical in the across-track direction near the edges of the swath (Figure 2). Along-track data density is dependent on survey speed and ping rate while across-track data density is primarily controlled by the angular spacing between successive sonar pings (Figure 2). With the Imagenex 881, the effective ping spacing is determined by the change in the user-defined angle (0.3° to 2.4°) of the mechanically scanning transducer between successive pings. The across-track spacing between soundings is smaller near nadir and larger toward the edge of the swath (Figure 2).

[16] Both size of the acoustic footprint and ping density affect the resolution of the resulting bathymetric maps. This is particularly important with

respect to resolving the details of the highly irregular seafloor common at MOR crests where vertical changes of meters are common over small horizontal distances. A small acoustic footprint size results from low-altitude surveys, and ensures that the multiple soundings are collected over small areas of the seafloor, thus increasing the resolution of the resulting bathymetric map. These data, however, can only be used to create high-resolution maps if the along-track spacing of soundings is sufficiently small.

[17] Near-bottom scanning sonar and pressure depth data were collected at the EPR 9°50′N during 29 *Alvin* dives conducted on five dive programs in 2004 and 2005 (2004, AT-11-07, AT-11-10, AT-11-13, AT-11-20; 2005, AT-11-26). The Imagenex transducer was mounted beneath the stern of *Alvin* in down-looking mode for all dives (Figure 3). Data were collected at 5 m altitude, with a sweep width of 90° (~10 m effective swath width), and at a slow vehicle speed (~0.25 knots; 0.13 m/s) to
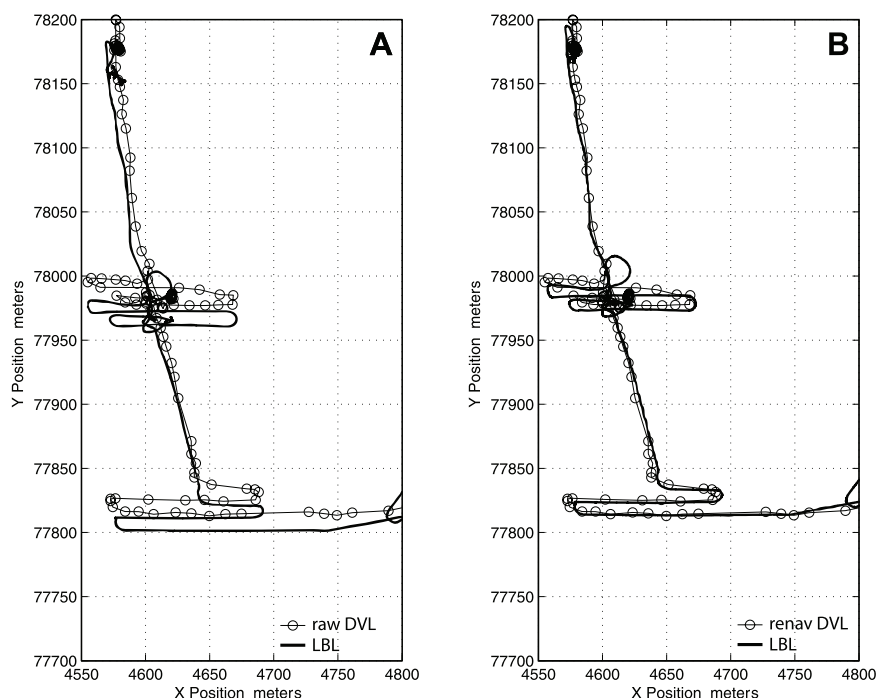
Figure 4. Renavigating Doppler velocity log (DVL) navigational data entails reintegrating Doppler velocities to create an X−Y track and then shifting the Doppler track to an edited LBL navigational track using a least squares fit [*Kinsey and Whitcomb*, 2004]. (a) Edited LBL fixes plotted with real-time DVL navigation track from *Alvin* dive 3973 (AT-11-07). (b) Edited LBL fixes plotted with renavigated DVL navigation track. Note that the renav DVL track has been shifted by as much as 10–15 m north and is more spatially consistent with the LBL navigation than the real-time DVL track.

provide a suitable balance between along-track and across-track resolution for creating submeters bathymetric maps (Figure 2). The across-track step size between pings was set to 2.4°, and at an average altitude of 5 m, the average ping rate was approximately 6 Hz. The high-resolution bathymetry data are coupled with visual observations of the seafloor.

[18] Previously reported ABE bathymetry data collected at 9°50′N with an Imagenex Model 881 675 kHz scanning pencil beam sonar [*Yoerger et al.*, 1996, 2002; *Fornari et al.*, 2004; A. Soule et al., manuscript in preparation, 2006] are used to reference our composite grids within the AST. The ABE data were acquired at speeds of ∼1 knot (0.5 m/s) at an altitude of ∼40 m along north-south survey lines spaced ∼60 m apart during two cruises on R/V *Atlantis* (AT7-4 (2001); AT7-12 (2002)) [*Yoerger et al.*, 1996, 2002; *Tivey et al.*, 1997, 1998; *Fornari et al.*, 2004; *Soule et al.*, 2005; Escartin et al., submitted manuscript, 2006] (Figures 1a and 1b). Details of sonar data acquisition and processing using ABE, are described by *Yoerger et al.* [1998, 2000]. The ABE bathymetry data are estimated to have positioning accuracy

better than ∼5 m [*Fornari et al.*, 2004] and were gridded at 5-m horizontal resolution [*Yoerger et al.*, 1996, 2002; *Tivey et al.*, 1997, 1998; *Fornari et al.*, 2004; *Soule et al.*, 2005]. The ungridded bathymetric data points, however, are of sufficient density to be gridded at 2 m (across-track, east−west) × 5 m (along-track, north−south) resolution (e.g., Figure 1b). Because of differences in the depth sensors used on ABE and *Alvin*, the ABE data presented here were shifted vertically by increasing the depth by 2 m in order to be regionally consistent with the *Alvin* depth measurements.

2.3. Data Processing Methods

2.3.1. Navigation

[19] *Alvin* navigational data were postprocessed for each dive using a suite of Matlab™ scripts principally authored by J. Kinsey, with contributions from L. Whitcomb, D. Yoerger, J. Howland, V. Ferrini, and others. This code is the focus of ongoing development, and the version used to process data reported here is available to all users of National Deep Submergence Facility (NDSF) vehicles via the NDSF data manager [*Ferrini et al.*,
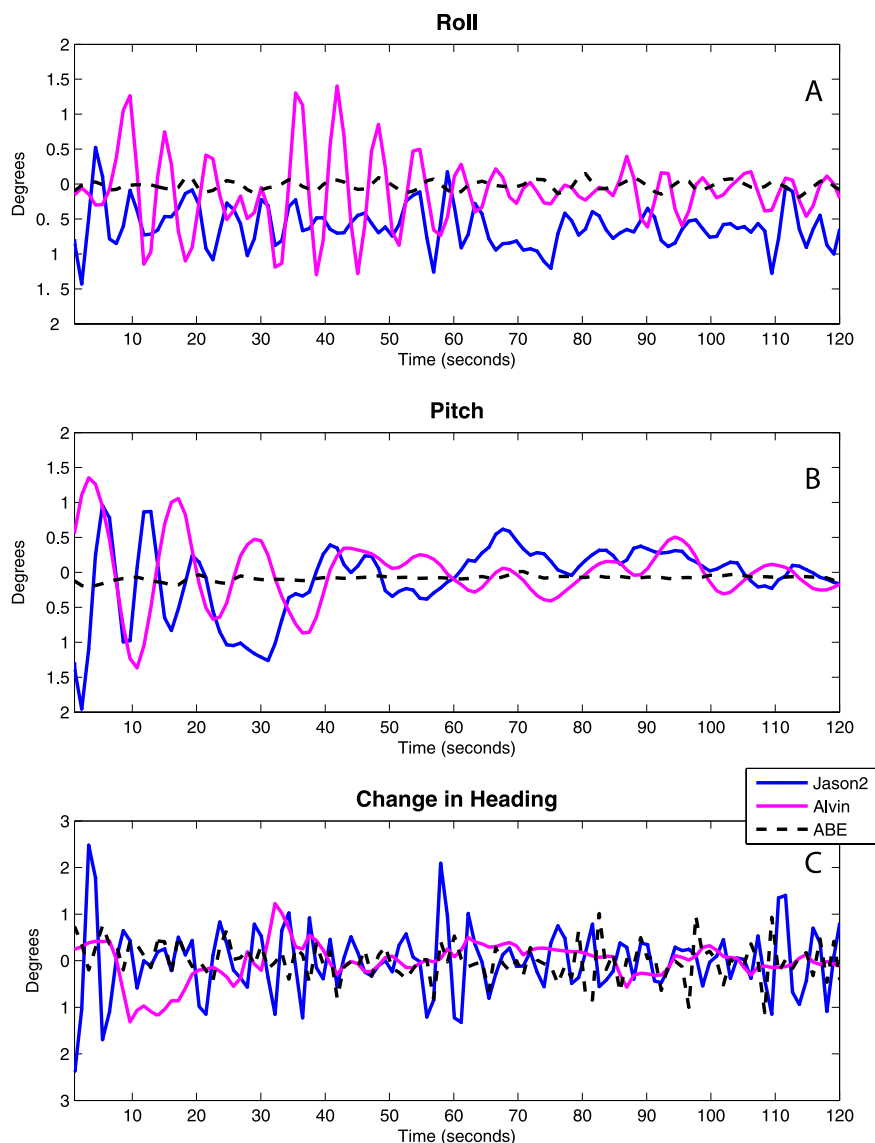
Figure 5. Example attitude (pitch, roll, change in heading) data from *Alvin*, Jason 2 ROV, and ABE AUV during typical bathymetric surveying operations. Note that the magnitude of (a) roll and (b) pitch variability with both *Alvin* and Jason 2 is larger than with ABE. (c) Change in heading is provided to illustrate the consistency of the survey lines for each vehicle.

2004, 2005a]. The processing pipeline permits manual editing of LBL fixes through a graphical user interface (GUI). Measured Doppler velocities are reintegrated to produce an X–Y track that is placed into a geographic coordinate frame through a least squares fit to the LBL track (Figure 4). The least squares solution used for the data presented here weights each LBL fix equally, applies a single X–Y offset to the entire Doppler navigation track, and therefore does not address time-varying errors in the data.

2.3.2. Bathymetry Data

[20] In addition to high-quality processed navigational data discussed above, accurate bathymetric soundings require accurate measurement of the motion of the survey platform (Figure 5). Because the instruments that record vehicle position and attitude data are mounted at different locations on the vehicle, precise measurement of the offsets between each sensor is important (Figure 3 and Table 1). These offsets are employed both in real-time through DVLNAV, and in the navigational postprocessing described in section 2.3.1.

Table 1. Positions of *Alvin* Sensors Used to Generate Bathymetric Maps Measured in Meters From The Vehicle Coordinate Frame Origin[a]

Sensor	X Position, m	Y Position, m	Z Position, m
Doppler Sonar	−6.55	0	−1.17
LBL Transducer	−0.71	0	−3.63
Paroscientific Depth Sensor	−2.92	+0.95	−0.76
Imagenex Sonar	−5.50	0	−0.10

[a] See Figure 3. The X axis is negative in the aft direction, the Y axis is negative toward port, and the Z axis is negative toward the top.

[21] Bathymetric maps were generated for each *Alvin* dive, by merging vehicle navigation and attitude data with traveltimes recorded by the sonar through a series of Matlab™ programs [*Ballard et al.*, 2000; *Singh et al.*, 2000; *Whitcomb et al.*, 2000; *Ferrini et al.*, 2004, 2005a]. Sonar data were windowed to remove data outside of a user-defined maximum range (25 m) and distance (20 m). An outlier removal program was then applied to remove data outside of a user-defined number (9) of standard deviations about a robust line fit of each sweep of the Imagenex. A tidal correction was applied to the bathymetry data (EPR tide range ~1 m) based on predicted tides generated with the SPOTL tide loading software [*Agnew*, 1996] to ensure that all bathymetric data were justified to the same vertical datum.

[22] Processed navigational data were used to place each Imagenex ping into a geographic coordinate system based on the position of the vehicle (x, y, z), the orientation of the scanning sonar transducer, and known offsets between the sensors (Figure 3)
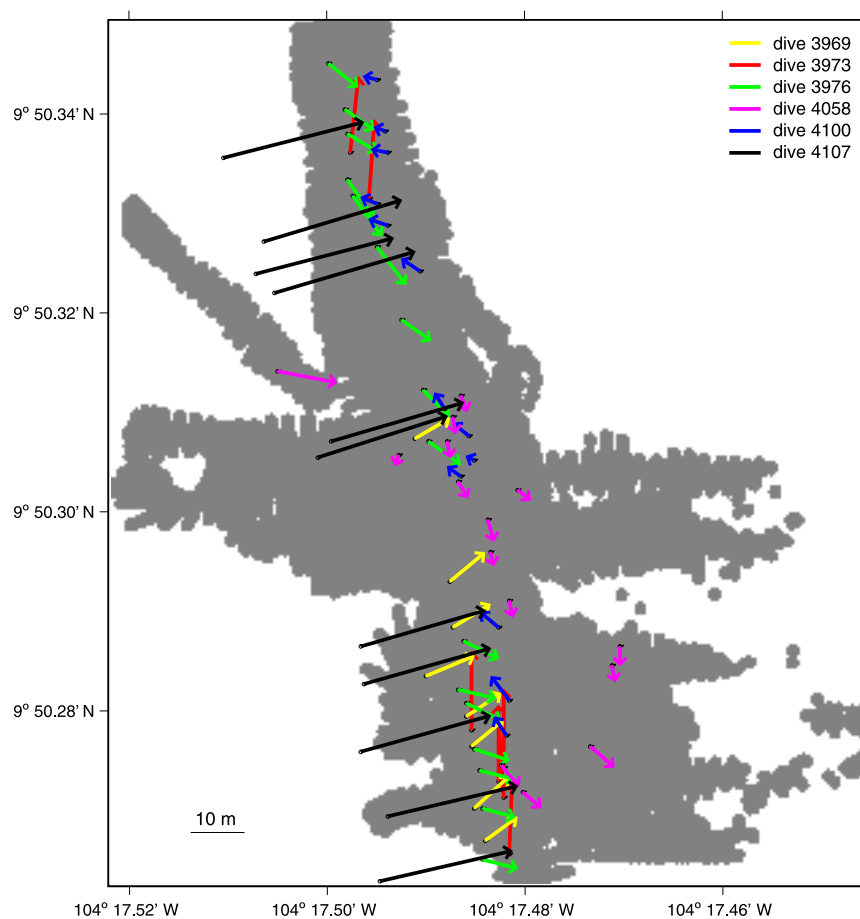

Figure 6a. Example spatial transformations required to create a composite grid of the Bio1 to P vent portion of the EPR (see Figure 1 for location). Note that seven dives were merged to create the composite grid and that spatial transformations were performed to merge six of them with the dive with the most extensive coverage (dive 3973). Each vector indicates the shift required for the corresponding ground control point (GCP), and colors correspond to different dives.
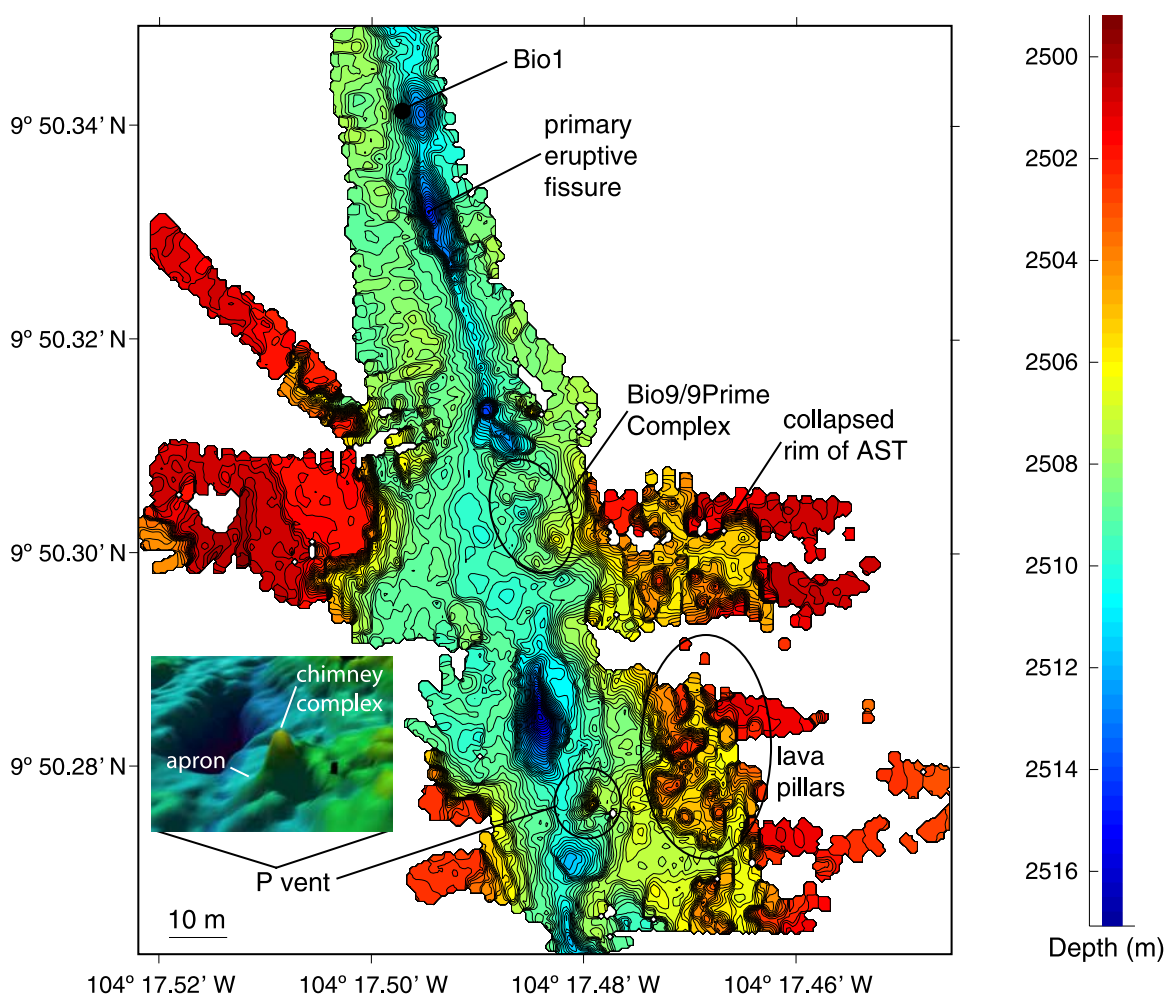
Figure 6b. Composite map (0.5 m horizontal grid cells; 0.25 m contours) created from seven *Alvin* dives conducted in 2004 and 2005. This map not only reveals the detailed morphology surrounding individual vent structures but also shows the well-defined primary fissure within the axial trough floor and a number of deep holes along it. The discontinuity of the primary fissure is in the region of hydrothermal activity is likely due to drainback [*Fornari et al.*, 2004]. An area of lava pillars with diameters of 1−2 m is evident among the collapsed and embayed eastern wall of the AST. The inset shows a three-dimensional perspective view of P vent (looking north) in which both the chimney complex and apron are resolved.

[*Singh et al.*, 2000]. Finally, a bathymetry editing GUI was created for the removal of remaining bathymetric outliers, for an additional level of quality control. Maps were generated for each dive at 0.5 m grid resolution using a weighted mean interpolation method with a Gaussian basis function (search radius: 0.75 m, sigma value: 0.5 m).

2.3.3. Grid Rectification

[23] A Matlab™-based grid rectification GUI was created to view gridded data on a per dive basis, and to manually identify at least five ground control points (GCPs) in each data set for spatial transformation of the original data points. High-

resolution (0.5 m grid) grids for each dive conducted within five vent areas along the EPR crest were used to select GCPs for each dive, and the one with the most extensive coverage was chosen as the base map for each vent area. A two-dimensional spatial transformation (linear conformal) was computed based on the GCPs selected for each dive (Figure 6a). The transformation was then applied to the ungridded bathymetry data points, and the shifted bathymetric data points for each dive were merged to create a composite grid (Figures 6b and 6c). Composite grids were repositioned and nested within 2 m × 5 m gridded maps of existing ABE bathymetry (X shifts, −43 to +15 m; Yshifts, −41 to +5 m).
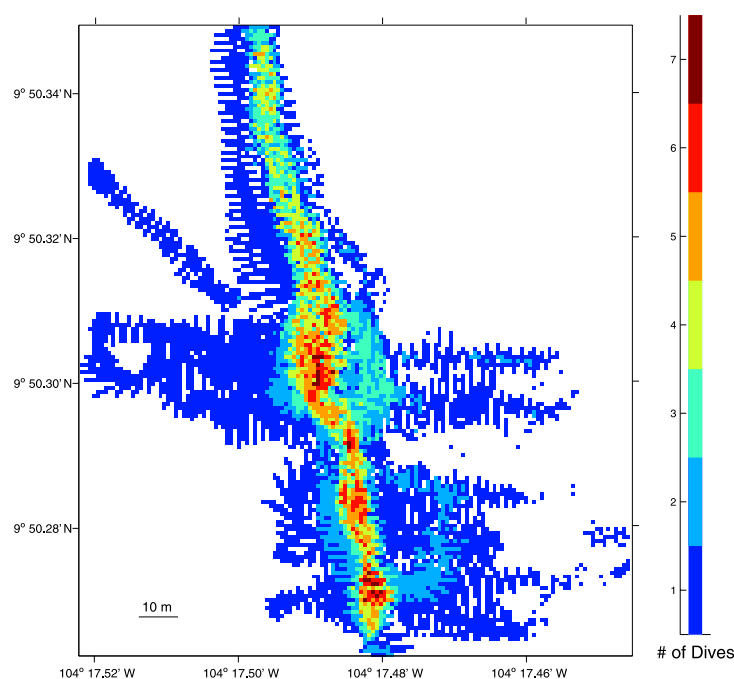
Figure 6c. Map of total overlap, indicating the number of dives from which data were contributed to each grid cell in the composite grid. In this example, data from seven dives were combined to create a 0.5-m gridded composite map. Note that most dives used in this composite map are concentrated within the center of the axial trough.
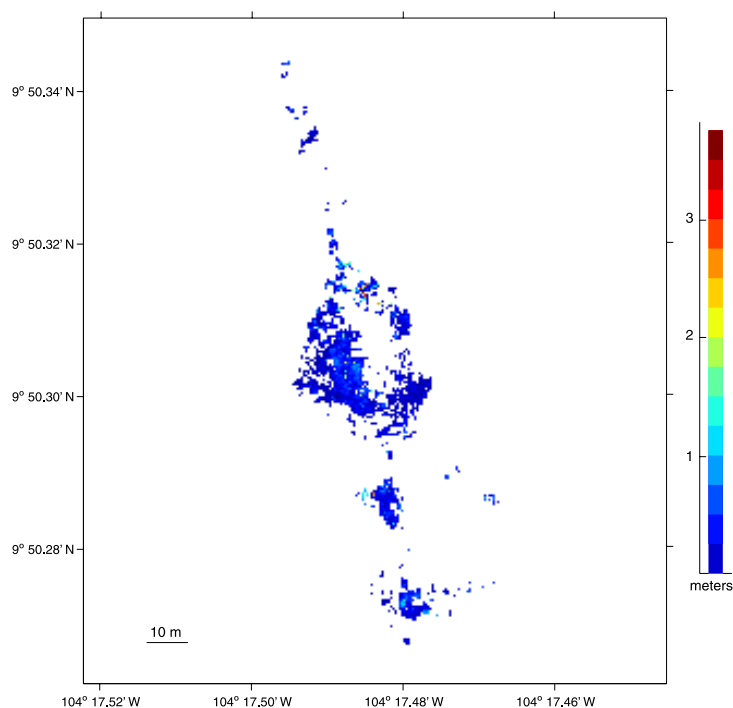

Figure 6d. Map of error metric (meters) for data shown in Figure 6a indicating the total thickness of the composite cloud of data points in grid cells with overlap [*Roman and Singh*, 2006]. This error metric treats data from each dive as a separate map and provides a measure of disparity between maps by considering the nearest-point distance between points contributed from each of the overlapping coverages. The median value based on the populated grid cells show here is 0.5, and the standard deviation is 0.5. Prior to running the grid rectification algorithm, calculating the same error-metric resulted in a mean value of 0.7 and the standard deviation of 1.2.
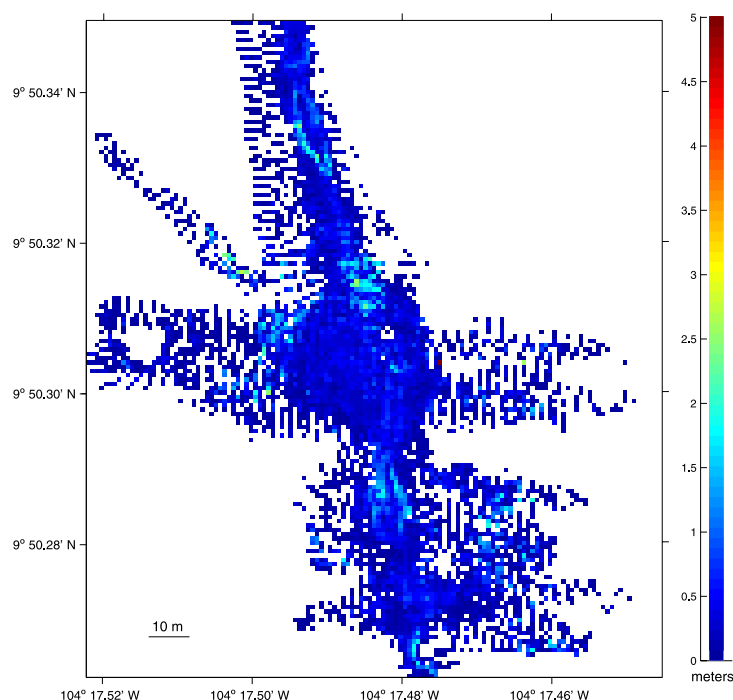
Figure 6e. Standard deviation of all bathymetric data points included in composite grid. Note that regions with larger values of standard deviation are focused around hydrothermal vent structures, the walls of the AST, and the edges of the primary eruptive fissure.

[24] For each high-resolution composite grid, we estimate a point-based error metric (Figure 6d) [*Roman and Singh*, 2006] and a binned standard deviation measure (Figures 6e–6j). The standard deviation was derived by binning all data points used in the composite grid and reveals larger values near vent structures and along the walls of the AST (Figure 6e). The error metric treats the data from each dive separately and for each bin is the average of multiple nearest point distance estimates between each of the overlapping maps. It therefore provides a measure of data disparity (e.g., thickness of the composite cloud of data points in meters) and can indicate the largest amount of misregistration between multiple overlapping maps (Figure 6d). Unlike the binned standard deviation measure the error metric is not biased by grid size, and therefore provides a more accurate bathymetric error estimate [*Roman and Singh*, 2006]. We utilize this information to ensure that data in the composite grids are consistent and do not exceed a local error of 5 m.

3. Results

[25] Five areas within the EPR axial trough between 9°49.9′N and 9°50.6′N had sufficient dive coverage for the creation of composite submeter

bathymetry grids. While conceptual drawings of the EPR AST that have been presented in several papers [*Fornari et al.*, 1998a, Figure 7; *Fornari and Embley*, 1995, Figure 20] have attempted to convey the complex nature of volcanic and hydrothermal features in the AST, these composite grids provide a quantitative display of the fine-scale bathymetric complexity of the AST based solely on sonar data rather than an artist's conception of a scientist's perceptions.

[26] The objectives for *Alvin* dives during which data were collected were focused on hydrothermal vent time series studies [*Shank et al.*, 2005; *Lutz et al.*, 2005; *Moore et al.*, 2005] and can therefore be used to locate biological and vent chemistry sample sites. In the discussion that follows for each site, we provide the basic microscale geological and morphological context of each site as resolved by the new high-resolution bathymetry. Where possible, this is supplemented with ground truth information in the form of selected seafloor images taken by *Alvin* or the TowCam deep-sea digital camera system [*Fornari and the WHOI TowCam Group*, 2003]. Vent areas are identified for each map area, and their locations (Table 2) have been revised based on the most recently acquired field data, and the morphology revealed in the compos-
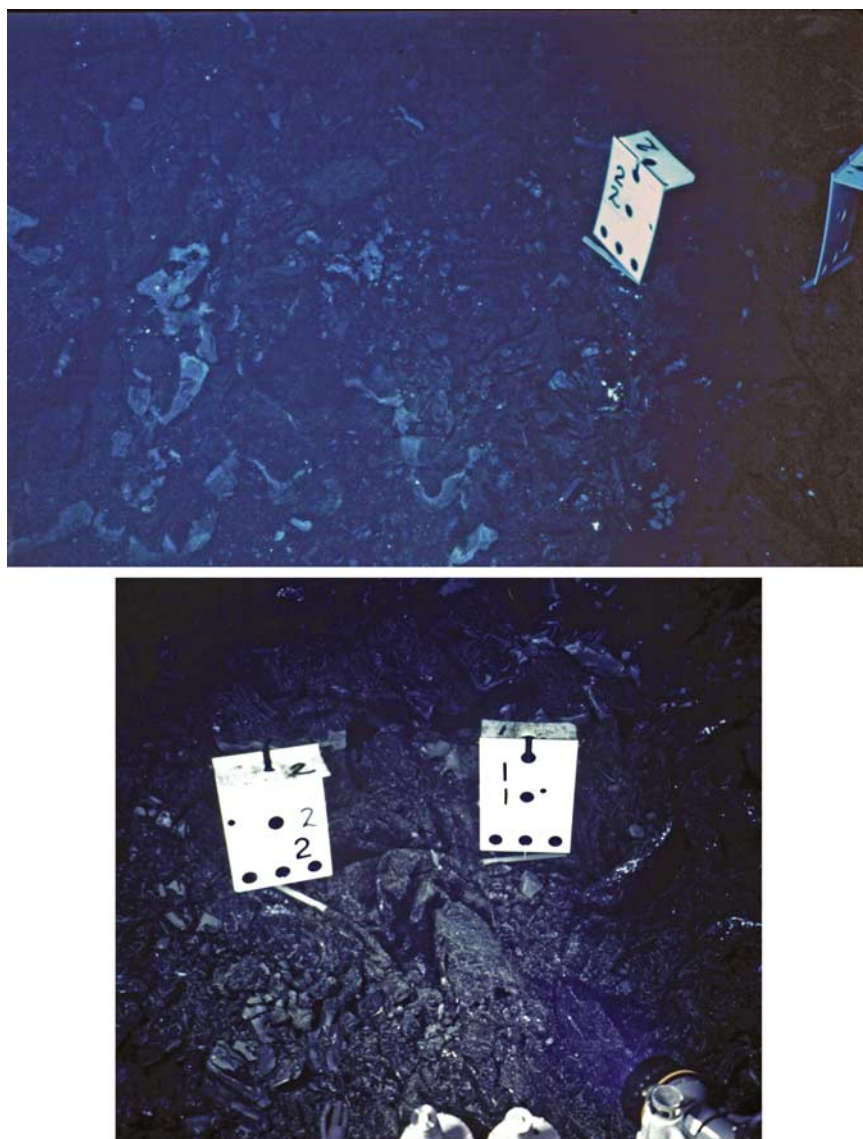
Figure 6f. *Alvin* 35 mm photographs taken of the AST floor near markers 1 and 2 [*Shank et al.*, 1998]. (top) Photograph of the view toward the south. The primary fissure is evident along left side of photograph. (bottom) Photograph showing close up of markers and jumbled sheet flow surface. Markers are 45 cm tall and 30 cm wide; holes in plastic have a diameter of 5 cm.

ite maps. All individual and composite bathymetry grids generated through this work, as well as revised vent locations, have been submitted to the Ridge2000 Data Management System (http://www.marine-geo.org).

[27] A median and standard deviation of error is provided for each composite map as an indication of the errors associated with the grid rectification algorithm. These values are based upon the error metric described in section 2.3.3 [*Roman and Singh*, 2006] (e.g., Figure 6b), and were calculated by considering only grid cells that contain data

collected during multiple dives. The median values and standard deviations for the error metric calculated on the data prior to grid rectification are also provided.

[28] It is noteworthy that the small-scale bathymetry of each of these sites has changed by varying amounts over the last 15 years since diving studies began in the EPR 9°50′N area in 1991 [*Haymon et al.*, 1993]. The changes are associated with repeated construction and collapse of vent sulfide chimneys (e.g., Bio9 and P vent), development of sulfide mounds (P vent), construction of new chimney

Figure 6g. Bathymetric complexity associated with the primary eruptive fissure of the 1991 eruption in the AST floor of the East Pacific Rise near 9°50′N. (top) Photograph of the east side of the fissure exposing flow sequences that are 20–60 cm thick separated by fragmented lava crusts. The two biomarkers (57, top, and 58, bottom) are 45 cm by 30 cm. (bottom) Photograph showing a view to the south of the deep, narrow primary fissure and sheet lava surface that dips into the axis of the fissure. The biomarker seen from the side is in middle of the photo. The scale across bottom of each photo is approximately 6 m (top) and 5 m (bottom). Both photos are frame-grabbed high-definition images (courtesy of W. Lange, WHOI, and R. Lutz, Rutgers University).

structures on lobate and sheet lava surfaces (e.g., Ty, Io and Tica hi-T vents), collapse and colonization within sheet and lobate lava along and adjacent to the primary fissure in the AST floor [*Shank et al.*, 1998; *Fornari et al.*, 1998a, 2004], and infilling of the primary fissure by collapsed sulfide structures and biological communities (e.g., at markers Bio9 and Bio119 [*Shank et al.*, 1998], see Figures 1a and 1b). Some of the associated biological, thermal and chemical changes at these sites have been detailed by *Shank et al.* [1998], *Fornari et al.* [1998b, 2004], *Von Damm* [2000], *Von Damm and Lilley* [2004], and *Scheirer et al.* [2006].

3.1. Geologic Context Derived From High-Resolution ABE Grid (2 m × 5 m) of the AST at 9°50′N

[29] In 1989, when the EPR axis near 9°50′N was first explored using the Argo II imaging and sonar system [*Haymon et al.*, 1991; *Fornari et al.*, 1998a], the AST was identified as a narrow feature with steep walls and complex bathymetry. The relief of the AST bounding walls was observed to be between 5 and 8 m based on near-bottom altimetry from *Alvin*, and in situ observations revealed that the plan view shape of the walls is notably scalloped rather than straight. These observations provided some of the first indications that
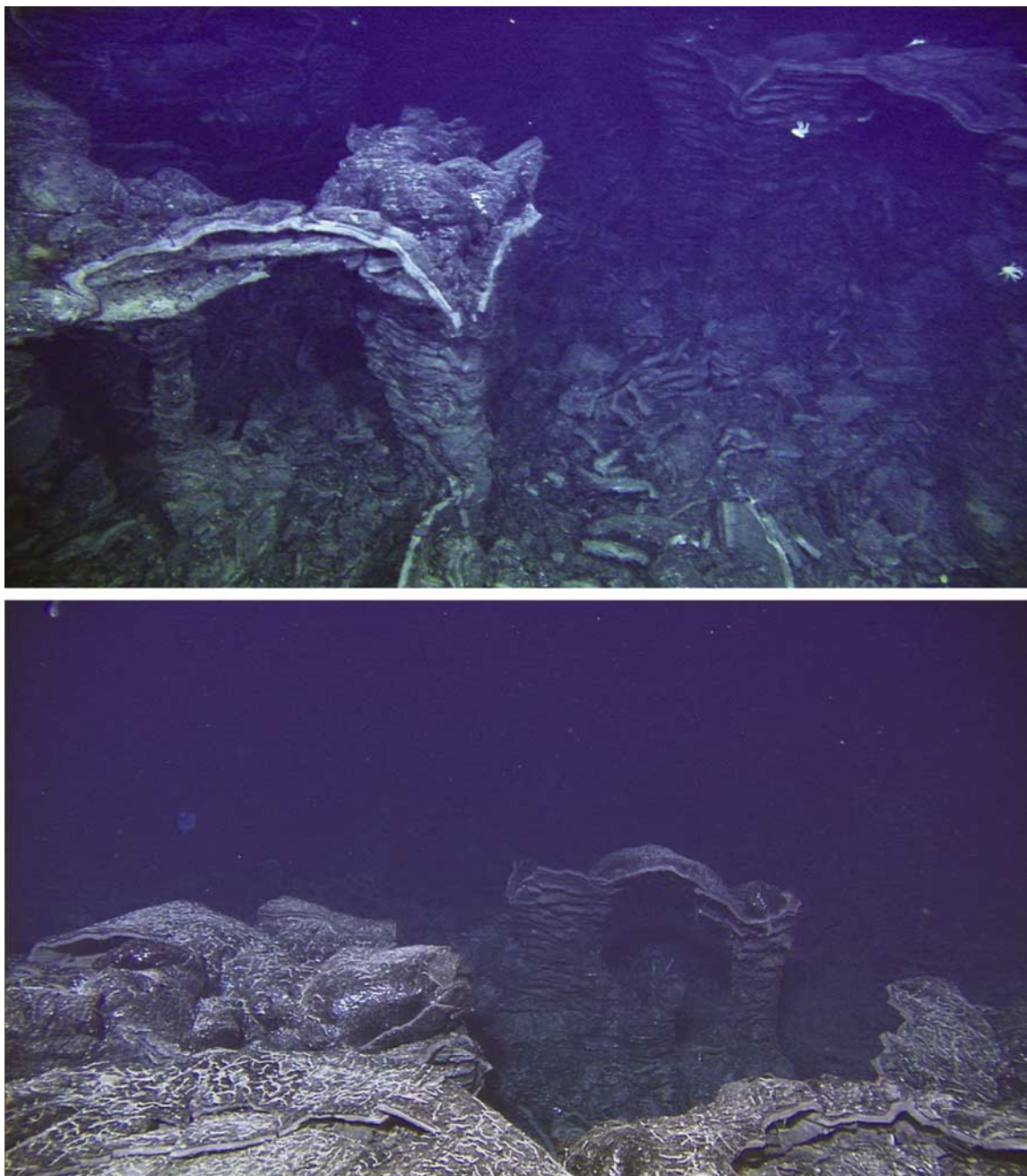
Figure 6h. Two views of the eastern margin of the axial summit trough (AST) in the 9°50′N area showing extensive collapse, lava pillars, and ramparts leading to the embayed character of the AST wall as depicted in Figure 6b. Distance across the bottom of the top photo is approximately 5 m, and that across bottom photo is approximately 4 m. Both photos are frame-grabbed high-definition images (courtesy of W. Lange, WHOI, and R. Lutz, Rutgers University).

the AST is a locus of volcanic collapse and that hydrothermal communities were common and perhaps most intense in the area around 9°50′N [*Haymon et al.*, 1991, 1993].

[30] The key morphological elements of the AST in the 9°50′N region (Figures 1a and 1b) are (1) the primary eruptive fissure, a 2- to 8-m-deep, linear anastomosing crack within the AST floor where the 1991–1992 eruptions were sourced, and (2) an extensive area of collapsed terrain with lava pillars and ramparts along the AST margin. A well-defined bathymetric gradient along the floor of the AST is evident over the ~1.8 km section
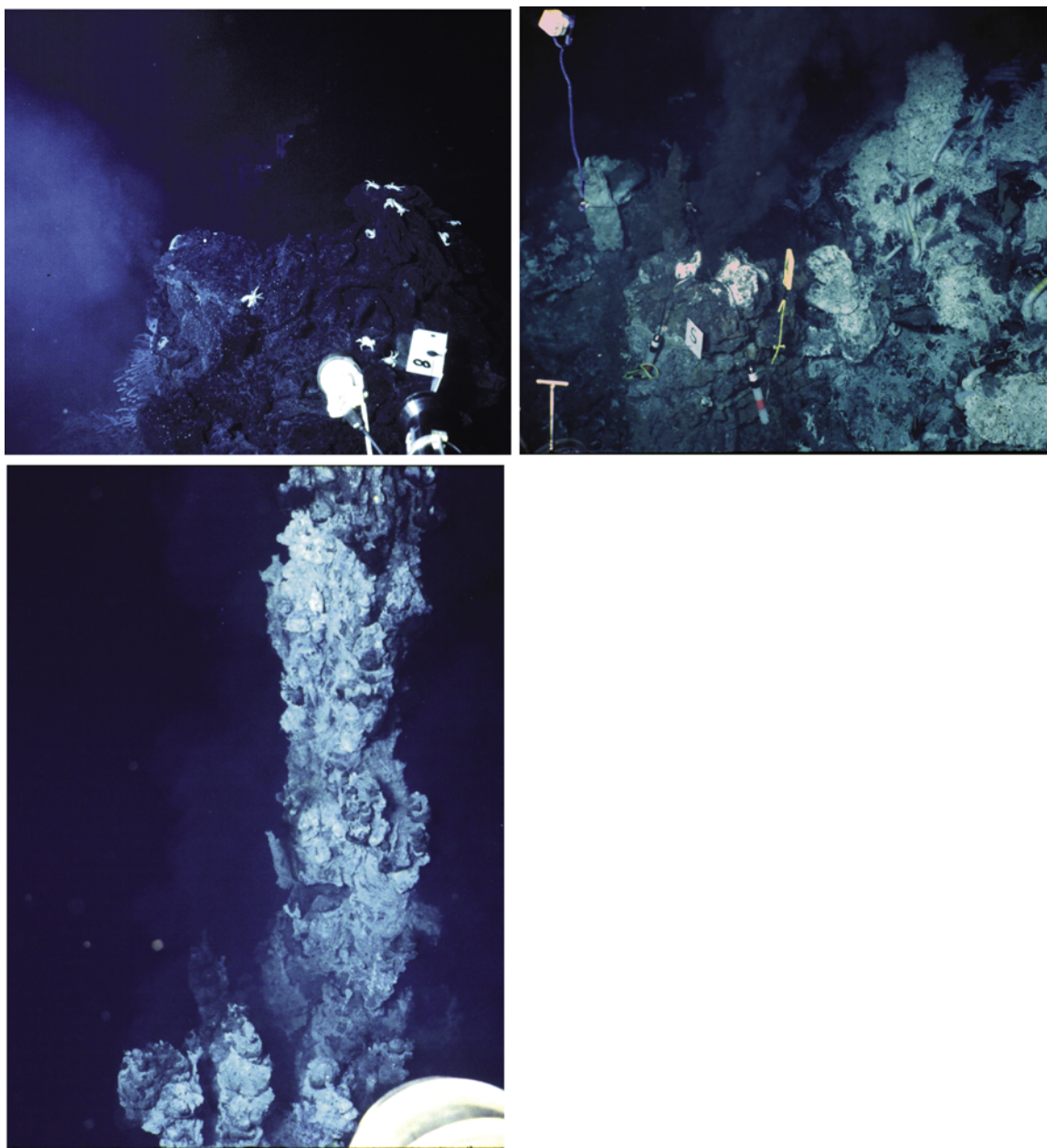
Figure 6i. *Alvin* 35 mm photographs of the Bio9 vent area. (top left) Photograph of the view looking south along the primary fissure with Biomarker 8 visible at lower right [*Shank et al.*, 1998]. Extensive diffuse venting along the primary fissure is evident from white cloud of smoke and *Tevnia* colonization along the fissure. (top right) Photograph showing the high-temperature Bio9 vent as it existed in 1993 with temperature loggers inserted into the active orifice [*Fornari et al.*, 1998b, 2004; *Shank et al.*, 1998, 2001; *Scheirer et al.*, 2006]. (bottom) Photograph showing the top ~3 m of one of the Bio9 chimneys as imaged in 2002. Scales across images in order described are ~4 m, ~3 m, and ~1.5 m, respectively. Although individual spires are not evident in the composite map (Figure 6b), hydrothermal mounds associated with the Bio9 complex are resolved.

shown in Figures 1a and 1b, with the northern area being ~20 m deeper than the area to the south. In a few locations, including south of 9°50.1′N (Figures 1a and 1b), the trough is shallow (<3 m) and it is difficult to resolve the edge of the trough from the chaotic collapsed terrain that flanks the AST on

either side. This area was presumed to have been partly filled by 1991–1992 lava with little drainback into the primary fissure. In contrast, the area to the north exhibits extensive drainback into the primary fissure at several locales, including areas
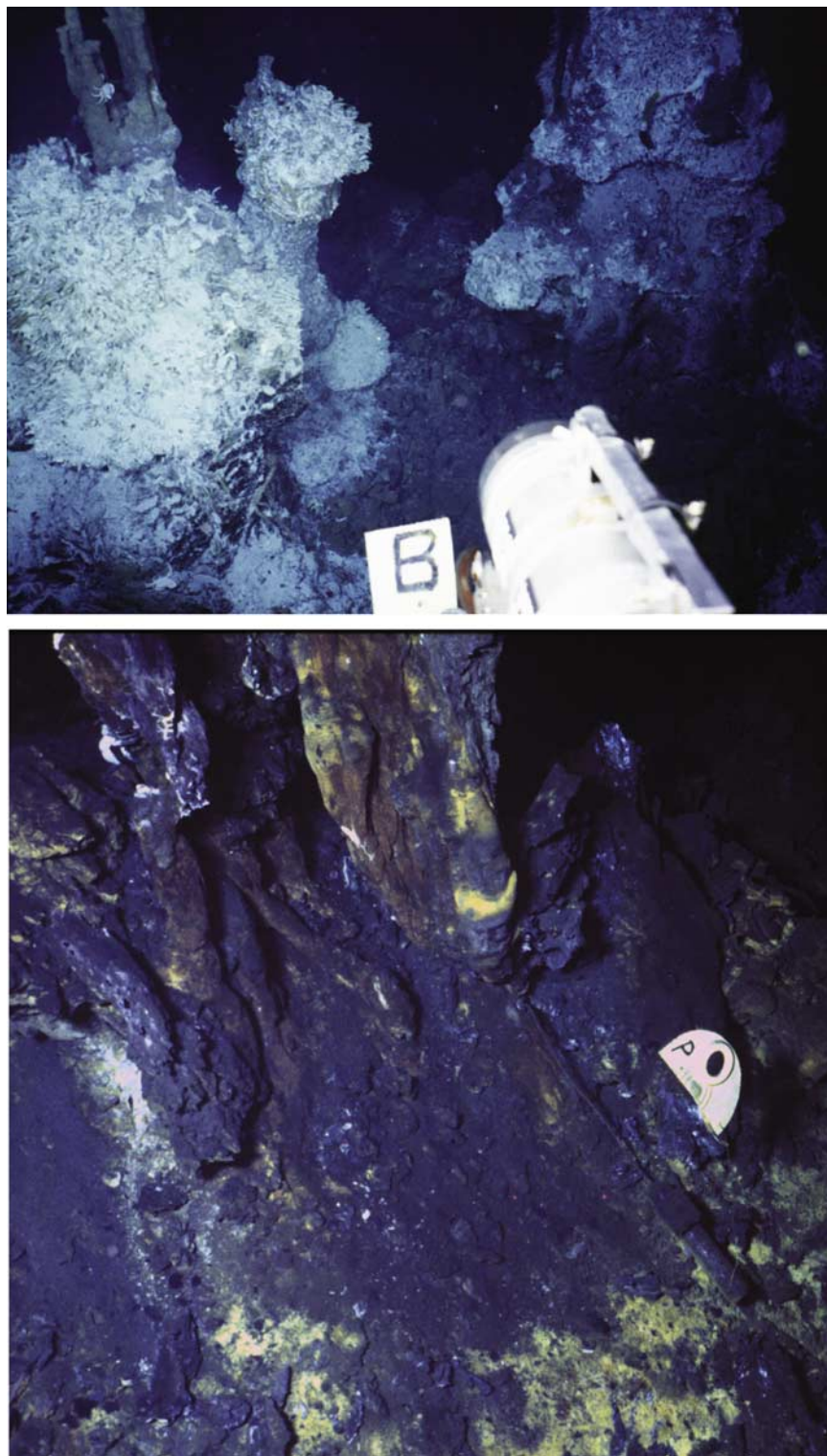
Figure 6j. *Alvin* 35 mm photographs of P vent. (top) Photograph showing the central and southern chimneys that form the P vent mound in the floor of the AST along the trace of the primary eruptive fissure. (bottom) Photograph showing base of one of the P vent chimneys at the south end of the mound that is traditionally sampled for fluids and temperature [e.g., *Von Damm*, 2000]. High-temperature logger that was deployed at the vent ~12 months prior is visible at lower middle right of image with "P" plastic bucket lid marker [*Scheirer et al.*, 2006]. Scale across top of left photo is ~5 m, and scale across base of right photo is ~1 m. The 0.5 m composite grid (Figure 6B) reveals the apron surrounding P vent as well as the tall hydrothermal spire.

Table 2. List of Vent Areas Based on Previously Reported Vent Locations (http://www.marine-geo.org) and Morphology Revealed in Composite Maps[a]

Vent Area	Latitude	Longitude	Approximate Size, m
Mussel Bed	9°50.5627′N	−104°17.5191′W	50 × 40
East Wall	9°50.5247′N	−104°17.5114′W	30 × 20
Tica	9°50.4108′N	−104°17.5000′W	20 × 10
Bio 1	9°50.3364′N	−104°17.4972′W	5 × 5
Bio 9	9°50.3023′N	−104°17.4874′W	25 × 15
P Vent	9°50.2713′N	−104°17.4820′W	20 × 20
Alvinellid Pillar/Ty/Io	9°50.1254′N	−104°17.4563′W	20 × 20
Bio 119	9°49.9323′N	−104°17.4252′W	30 × 20

[a] Note that positions are provided for the center of vent areas identified in the composite maps. The approximate size of the vent area around each position is also provided.
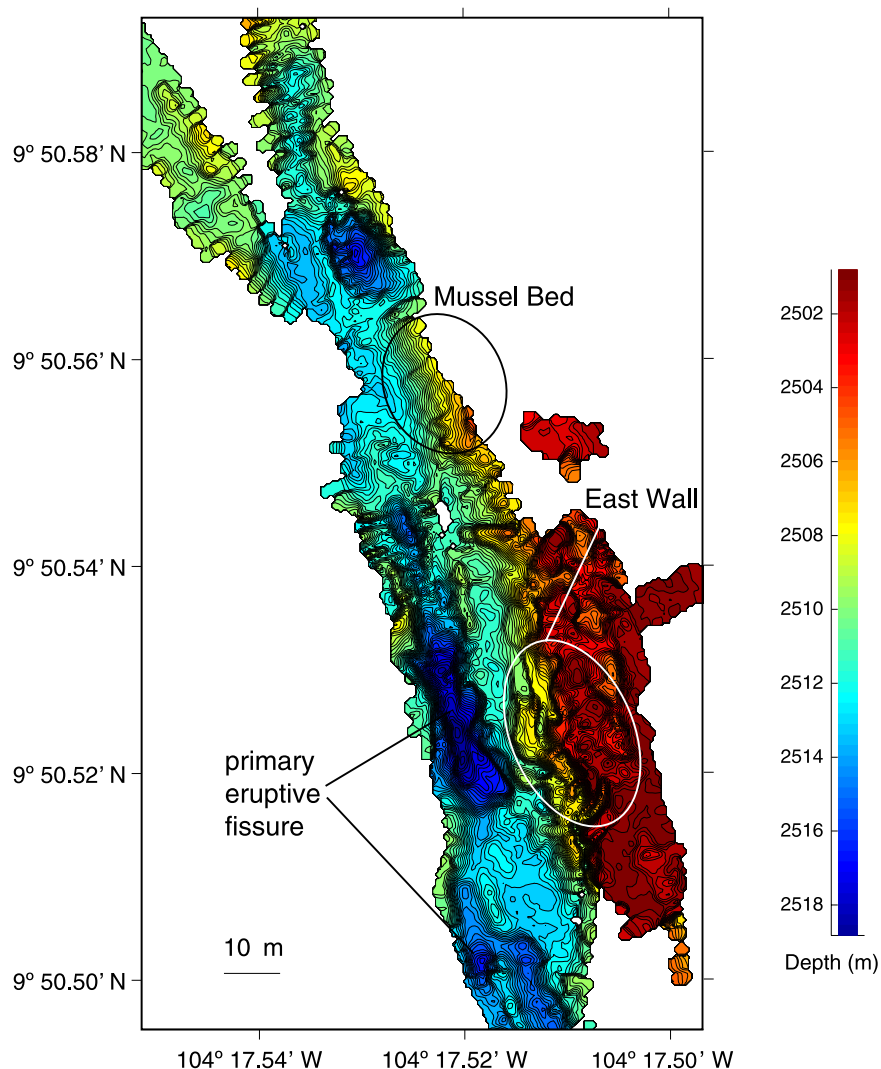

Figure 7a. Composite map (0.5 m grid, 0.25 m contours) of the EPR near the Mussel Bed and East Wall biological communities near 9°50.5′N. This map was created with data collected during nine dives in 2004 and 2005. The primary fissure at this site is at least 6 m deep and is well-defined and continuous in the region of hydrothermal activity. The eastern wall of the AST is characterized by areas of extensive collapse. The median of the error metric calculated for this grid is 1.3 m, while the standard deviation of the error metric is 1.4 m (median 4.4, SD 4.4 before rectification).
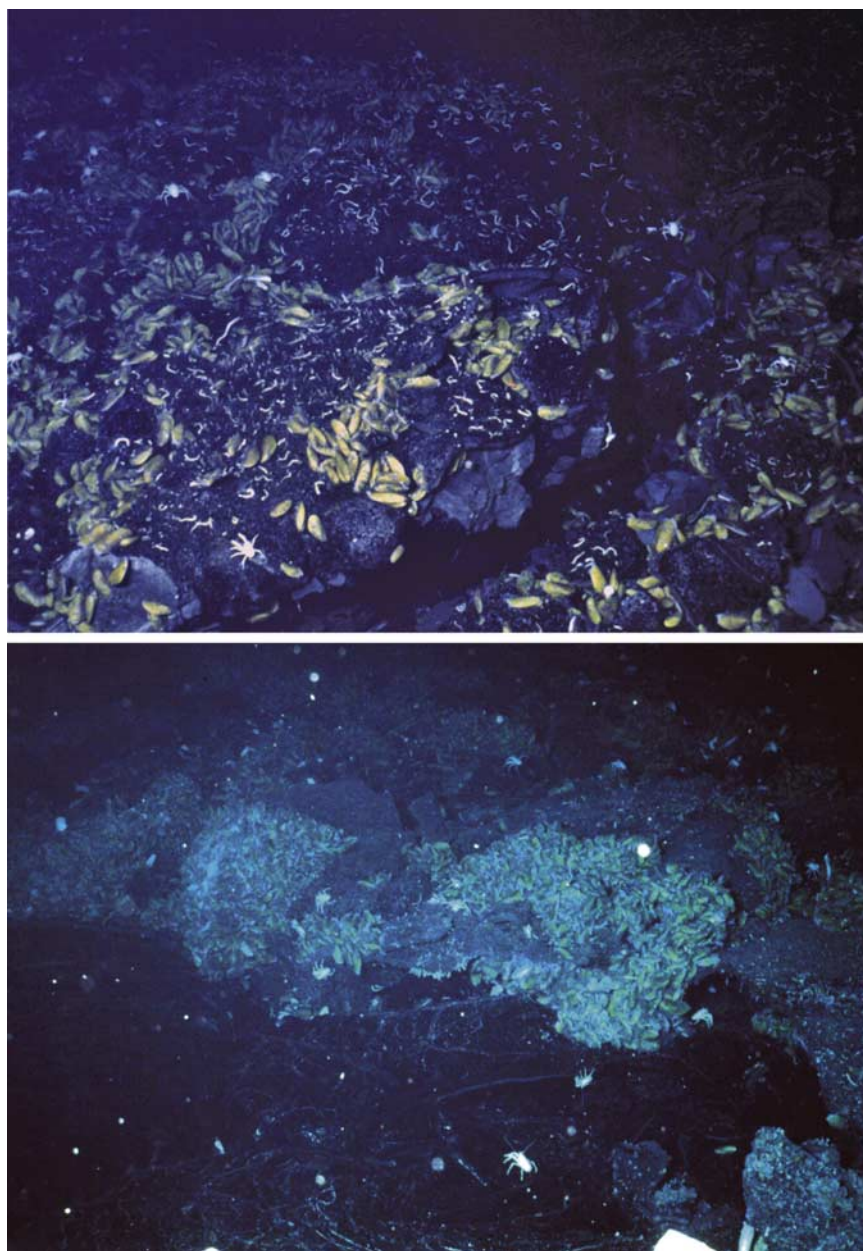
Figure 7b. *Alvin* 35 mm photographs taken in 1991 and 1992 (dives 2351 and 2498) of the Mussel Bed area. (top) Photograph showing extensive mussel community and serpulid worms (small white curvy features on the basalt surface). (bottom) Photograph showing the Mussel Bed site just after or during the 1991 eruption with the new, black 1991 lava flow in the foreground of the photo lapping onto older lobate flows covered with mussels. Distance across bottom of top photo is ∼2 m, and that across bottom photo is ∼4 m.

proximal to the high-temperature vents [*Fornari et al.*, 2004].

3.2. Mussel Bed, East Wall

[31] In 1989, the first comprehensive survey of the EPR axis near 9°50.55′N using the ARGO imaging system [*Haymon et al.*, 1991] documented two areas of active diffuse flow, colonized by vent endemic megafauna (Figures 7a,

7b, and 7c). Mussel Bed is a ∼40 m by 50 m area (9°50.59′N, −104°17.52′W) predominantly outside the AST, colonized by mussels and surrounded by serpulid worms on variably collapsed lobate lava. The East Wall area (9°50.54′N, −104°17.51′W) is a section of the eastern AST (Figures 7a, 7b, and 7c) that has extensive diffuse flow and animal aggregations over a ∼30-m-long section of the AST wall, primarily on benches created by lava still-
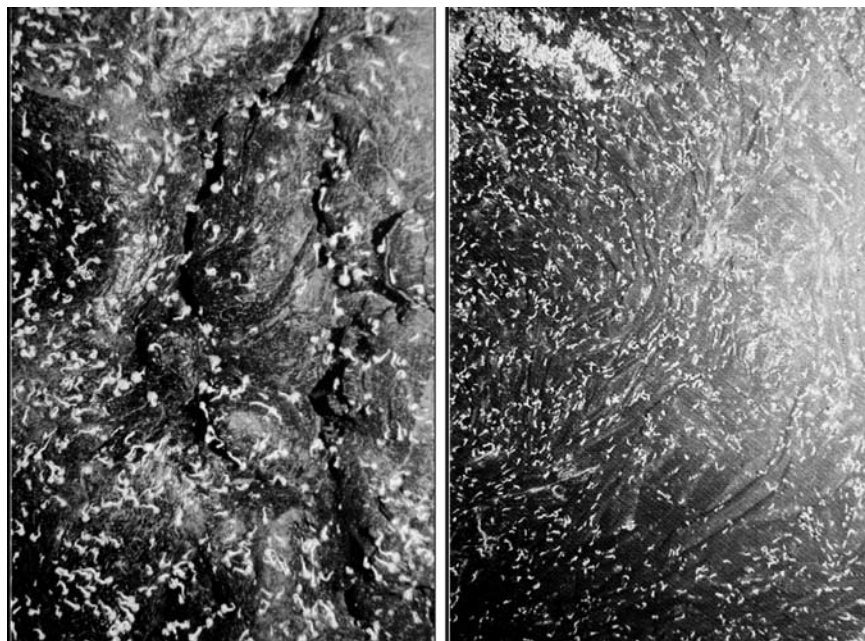
Figure 7c. Argo electronic still camera images taken in 1989 [*Haymon et al.*, 1991] of the area around Mussel Bed (Argo-97, left) and of the sheet flow terrain within the adjacent axial summit trough (AST) floor (Argo-95, right). In Figure 7c (right), small tubeworm communities are visible at upper left. Scale across bottom of each image is ∼2 m (left) and ∼4 m (right).

stands, pillar ramparts and talus piles. Communities of tubeworms have been overgrown by mussels, both at the base and top of the eastern AST wall since ∼2001. The diffuse hydrothermal flow at East Wall continues to be elevated relative to Mussel Bed as of the last visit to these sites in 2005.

[32] The AST near Mussel Bed and East Wall is approximately 45 m wide and 10 m deep (Figures 1a and 1b), although it is not fully imaged in the composite grid (Figure 7a). The bathymetry of the AST is complex, and the primary fissure is up to 6 m deeper than the floor of the AST. An area of collapsed terrain proximal to the eastern AST wall (Figure 7a, East Wall) is composed of lava pillars and ramparts of coalesced lava pillars [e.g., *Gregg et al.*, 1996; *Chadwick*, 2003]. The collapse features and lava pillars result in localized bathymetric variability on the order of 2 to 4 m over horizontal scales of less than 5 m (Figure 7a). The biological communities of East Wall and Mussel Bed are located within this collapsed and lobate terrain along the eastern margin of the AST (Figures 7a, 7b, and 7c).

3.3. Tica

[33] The Tica hydrothermal area (9°50.41′N, −104°17.50′W) is located along the center of the AST floor in lobate/sheet lava terrain and among collapsed/pillar structures along the eastern margin of the AST (Figure 8a). Just after the 1991 eruption, the Tica area was a source of diffuse venting directly from the lobate/sheet flows emplaced during the eruption. This vent area has been dominated by *Riftia* tubeworms. In 2005, the Tica area continued to be a source of sustained diffuse flow and mussels now occupy habitats on the floor of the AST and on the pillar-rich margin of the eastern AST wall (Figure 8a). Higher-temperature effluent is also evident in the southeastern margin of the field near the eastern AST wall where a 0.25-m-tall sulfide deposit, built on a 6-m-long linear, E−W trending tumulus covered with *Riftia* tubeworms, is venting fluids over 340°C (*Alvin* high-temperature probe measurements in 2004 (K. L. Von Damm, unpublished data, 2004)).

[34] The AST near Tica is as wide as 45–60 m, and the walls are 5 m tall (Figures 1a, 1b, and 8a). The well-defined primary fissure is located near the center of the AST and is roughly 10 m wide and up to 8 m deeper than the broad floor of the AST (Figure 8a). Toward the northern end of the hydrothermally active area, the primary fissure widens to 20 m and bifurcates. Figure 8a shows a characteristic morphology for a section of the AST encompassing a ∼50- to 60-m-wide AST floor with undulating microbathymetry having up to
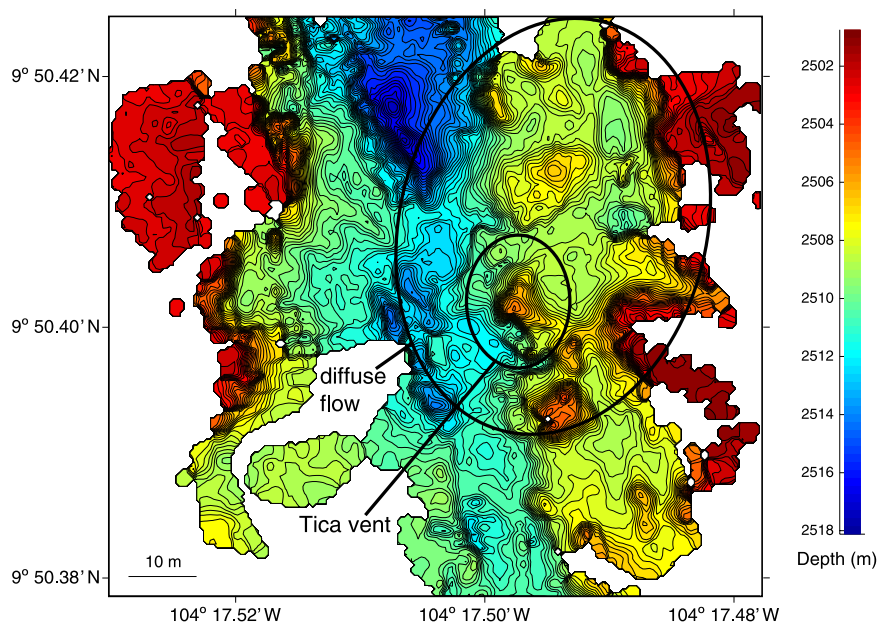
Figure 8a. Composite map (0.5 m grid, 0.25 m contours) of the area surrounding Tica vent created with data from 9 *Alvin* dives conducted in 2004 and 2005. The median value of the error metric calculated for this composite map is 0.6 m, and the standard deviation is 0.7 m (median 1.5, SD 1.6 before rectification). The largest estimated errors are induced by navigational offsets on the order of a few meters near abrupt bathymetric boundaries (e.g., trough wall and/or vent structures).

5 m of local relief, flanked by steep, nearly vertical AST walls which are extensively embayed as a result of collapse that ensued after the last (1991–1992) drainback event. For the Tica area, the eastern AST wall appears to have a narrow step (20–25 m width) that serves as a platform for lava pillars and small hydrothermal mounds. The high-temperature chimney is localized on a small mound (7 × 7 m) that is roughly 3 m taller than the adjacent seabed (Figures 8a and 8b). The primary fissure, evident in the middle to northern portion of the map shown in Figure 8a, appears to be partly paved over, perhaps by late stage drainback, in the southern part of this area.

3.4. Bio9 Vent to P Vent Complexes

[35] Chimneys associated with two high-T vent areas in the northern limit of the BioTransect [*Shank et al.*, 1998], the Bio9/Bio9prime and the P vent sites, developed subsequent to the April 1991 volcanic eruption. Bio9/9prime and P vent are located near the middle of the AST along the trace of the primary fissure and ~40 m apart [*Haymon et al.*, 1993; *Shank et al.*, 1998; *Fornari et al.*, 1998b; *Von Damm*, 2000; *Von Damm and Lilley*, 2004; *Scheirer et al.*, 2006], and are evident in the composite grid (Figure 6b). Bio9prime and Bio9 vents (9°50.32′N, −104°17.48′W) are located

within a few meters of each other along the primary eruptive fissure [*Haymon et al.*, 1993; *Fornari et al.*, 1998a, 1998b].

[36] The P vent chimneys (9°50.30′N, −104°17.49′W) are located along the primary eruptive fissure ~40 m south of Bio9 atop a sulfide mound that is several meters high (Figure 6b). The general character and setting of these vents within the AST have been discussed by *Haymon et al.* [1993], *Fornari et al.* [1998b, 2004], and *Shank et al.* [1998]. *Shank et al.* [1998] provide the most comprehensive description of the biological community structure of this segment of the AST near 9°50′N (Figure 6b) and the physical setting of the animal communities in relation to the AST walls and primary fissure. *Von Damm* [2000] and *Von Damm and Lilley* [2004] discuss the high-temperature and diffuse flow venting and the chemistry of the fluids from these vents.

[37] The high-resolution bathymetry shown in Figure 6b provides a new perspective of several morphological characteristics of the AST and how they relate to both volcanic and hydrothermal processes. The AST is ~45 m wide, and the well-defined primary fissure is up to 10 m wide and 7 m deeper than the floor of the AST. The linearity and continuity of the primary fissure is disrupted in the vicinity of Bio9/Bio9prime and P vent (Figure 6b).
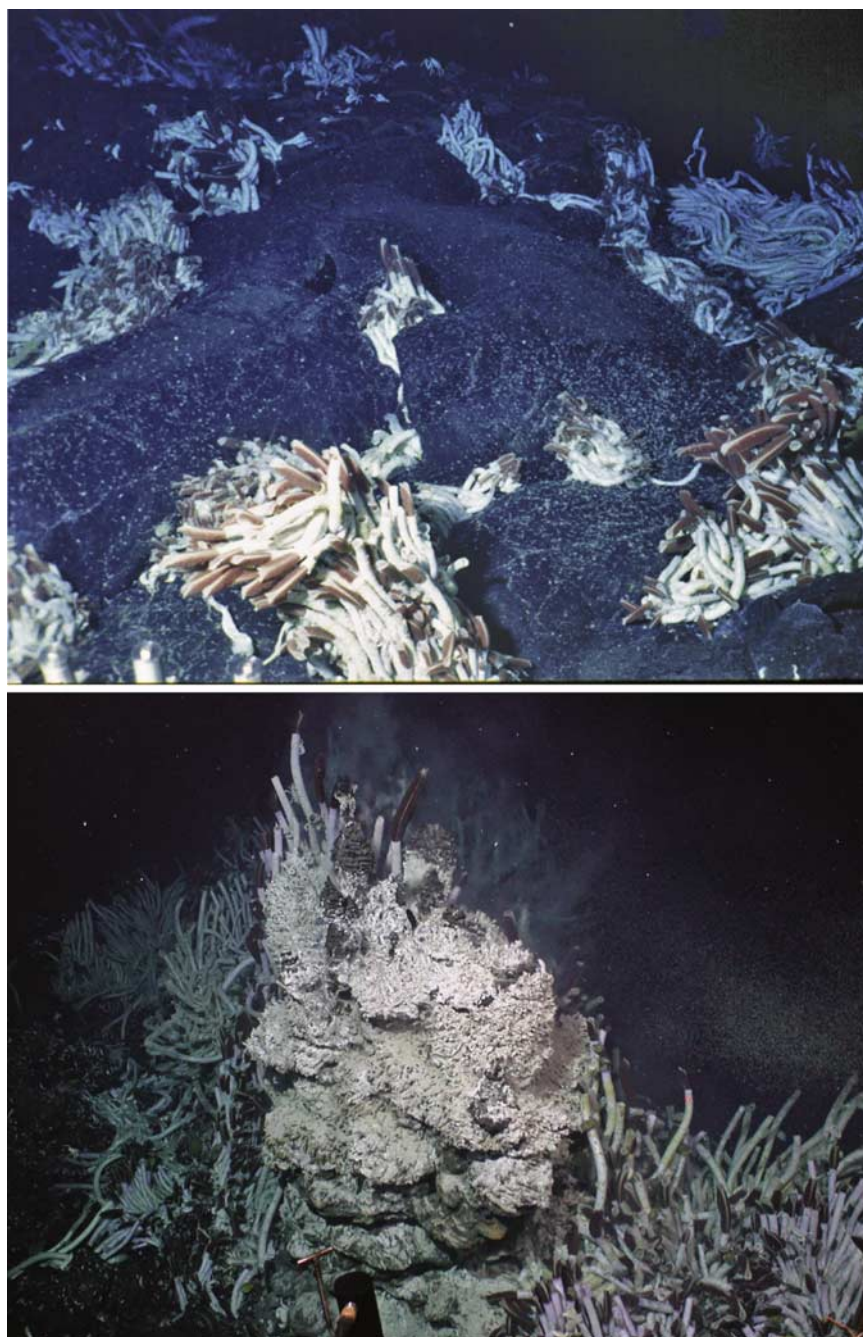
Figure 8b. (top) *Alvin* 35 mm photograph of the axial trough floor in the vicinity of Tica vent as imaged in 1994 showing extensive *Riftia* communities developed in interstices with lobate lava. (bottom) An electronic still camera image taken in 2004 of the high-temperature chimney at the southern end of Tica field that has been active since 1996.

In situ observations from *Alvin* have identified extensive evidence for drainback along the length of the primary fissure, which is likely the cause of the discontinuity [*Fornari et al.*, 2004]. The complex terrain associated with the eastern AST wall near the vents is dominated by collapsed areas that are up to 6 m deeper than the adjacent seafloor. Hydrothermal structures (2–4 m tall) associated with both P vent and Bio9/9prime are identifiable in the composite grid (Figure 6b). Individual lava pillars with heights of up to 2 m are also identifiable
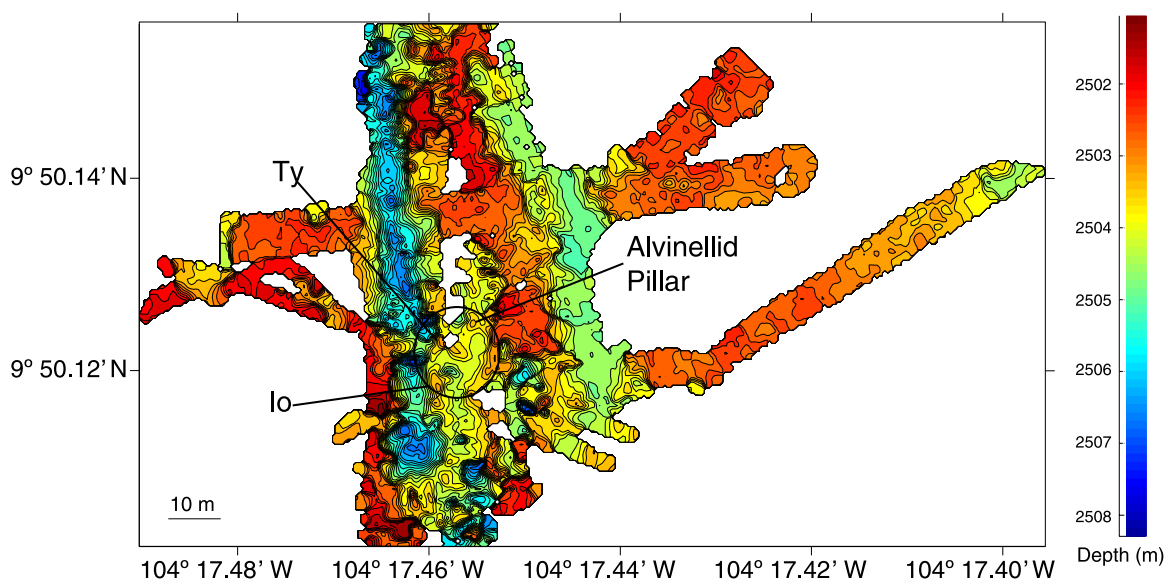
Figure 9. Composite map (0.5 m grid, 0.25 m contours) of EPR axial summit trough around the Alvinellid Pillar vent created with data from seven dives conducted in 2004 and 2005. The region of hydrothermal activity associated with Ty, Io, and Alvinellid Pillar is indicated by the circle, and the lines provide a relative indication of their locations within the circle. Note that the AST is ∼45 m wide but is divided by a 20 m wider bathymetric high (∼2−3 m tall). Hydrothermal activity is focused on the western margin of this high. The median value of the error metric calculated for this grid is 0.9 m, and the standard deviation is 1.05 (median 1.3, SD 1.1 before rectification).

within the collapsed region of the AST's east wall (Figure 6b).

3.5. Marker 82 (Alvinellid Pillar, Ty, and Io Vents)

[38] The Alvinellid Pillar vent area (9°50.12′N, −104°17.44′W; Figure 9) lies on the margin of the east AST wall and is a narrow hydrothermal chimney that grew out of lobate lava prior to the 1991 eruption (fresh, 1991 lava was observed lapping to the margins of the base of the chimney on *Alvin* dive 2350) [*Haymon et al.*, 1993; *Shank et al.*, 1998]. *Riftia* tubeworms (∼1 m long) and alvinellid polychaetes were documented at the base of this structure less than a month following the eruption [*Shank et al.*, 1998]. The vent has been active ever since, even after it fell to the north from its now active base in 2002. Alvinellid polychaetes communities dominate the walls of the active chimney, and *Riftia* communities occupy the base and the less active walls of the chimney. The seafloor expression of high-temperature venting in this area changed dramatically in 1996, when two chimneys "Ty" and "Io" [*Von Damm and Lilley*, 2004], emerged from fractures in the AST floor within an area less than 15 m west of the Alvinellid Pillar [*Shank et al.*, 1998].

[39] Although the AST near Ty, Io, and Alvinellid Pillar is roughly 45 m wide, it is divided into two parallel troughs by a 2-m-tall bathymetric high that is approximately 20 m wide (Figure 9). Hydrothermal activity is focused on the eastern edge of the westernmost trough, and sulfidic chimneys are constructed along the in-filled primary fissure, probably reflecting posteruption drainback and collapse (Figure 9). The AST is shallow (2−4 m), and contains several 1- to 1.5-m-deep pits along the primary fissure (Figure 9). Like the Tica vent area, the AST is characterized by a narrow (<10 m wide) bathymetric step upon which hydrothermal activity is focused (Figure 9). The eastern wall of the AST is also characterized by coalesced lava pillars on the order of 1−2 m in height (Figure 9).

3.6. Marker Bio 119

[40] Extensive, diffuse hydrothermal flow (∼<25°C [*Shank et al.*, 1998; *Fornari et al.*, 1998b]) was observed in the marker Bio119 area (9°49.94′N, −104°17.41; Figures 10a and 10b) during the 1991 eruption issuing from the primary fissure in this segment of the AST. Time series biological observations have been made of the Bio119 biological communities since 1991 [*Shank et al.*, 1998]. *Riftia* assemblages that were identified in 1993 (Figure 10b) were dominated by mussels in 1995.
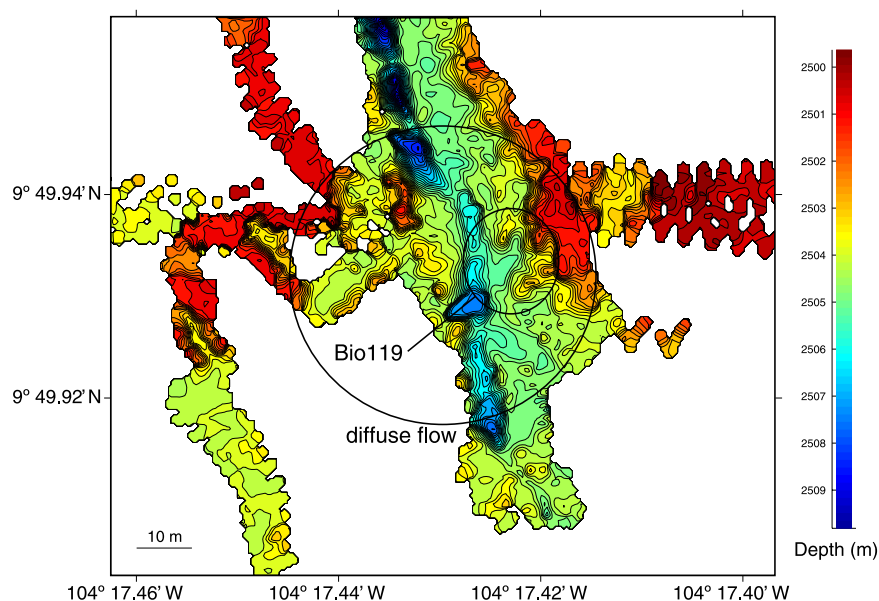
Figure 10a. Composite map (0.5 m grid; 0.25 m contours) of the area surrounding marker Bio119, generated with data from nine dives (2004 and 2005). The large area of diffuse flow at this site extends from the primary fissure in the axial trough floor to the eastern and western walls. The region of focused flow is located along the primary fissure in the floor of the AST and is indicated as Bio119. The primary fissure in the center of the AST is well-defined, continuous, and narrow. Data coverage of the walls is less extensive than at other sites, but collapse features are evident along both the east and west walls. The median of the error metric calculated for this grid is 0.4 m, and the standard deviation of the error metric is 0.4 m (median 0.8, SD 1.2 before rectification).

The mussel assemblages, present on lobate lava forming the margin of the primary eruptive fissure in 1994, extended from the eruptive fissure and adjacent 1- to 3-m-tall lava pillars (as shown by the isolated closed contour highs seen in the AST floor in this area; Figure 10a), to the western bounding wall by the end of 1995 [*Shank et al.*, 1998]. Over the past decade, mussel colonization has continued to the extent that the primary fissure is now nearly filled with mussels. As part of the Ridge2000 program, the mussel communities in this area have been the focus of manipulative integrated studies linking diffuse fluid chemistry, microbial community structure, and faunal colonization [*Shank et al.*, 2005; *Lutz et al.*, 2005; *Moore et al.*, 2005].

[41] The AST in this region is broad (~40 m wide) and shallow (<4 m deep) (Figure 10a). Immediately south of Bio119, the AST widens to approximately 100 m with a small breakout along the western margin (Figures 1a and 1b). The primary fissure is continuous and roughly 5 m wide and 1−4 m deep (Figures 10a and 10b). The AST floor west of the primary fissure is complex and characterized by a number of structures with heights on the order of 0.5−2 m (Figure 10a). Bio119 is located along the eastern margin of the

Figure 10b. *Alvin* 35 mm photograph of the Marker 119 diffuse flow community developed within the primary eruptive fissure of the 1991 eruption in the floor of the EPR axial trough. View is to the NW with primary fissure in the foreground of the photo. Extensive *Riftia* and *Tevnia* tubeworm colonization is evident along the lip of the fissure. Marker Bio119 is 45 cm tall and 30 cm wide. Bathymetric mounds like the one seen here are evident within the Bio119 region identified in the composite map (Figure 10a).
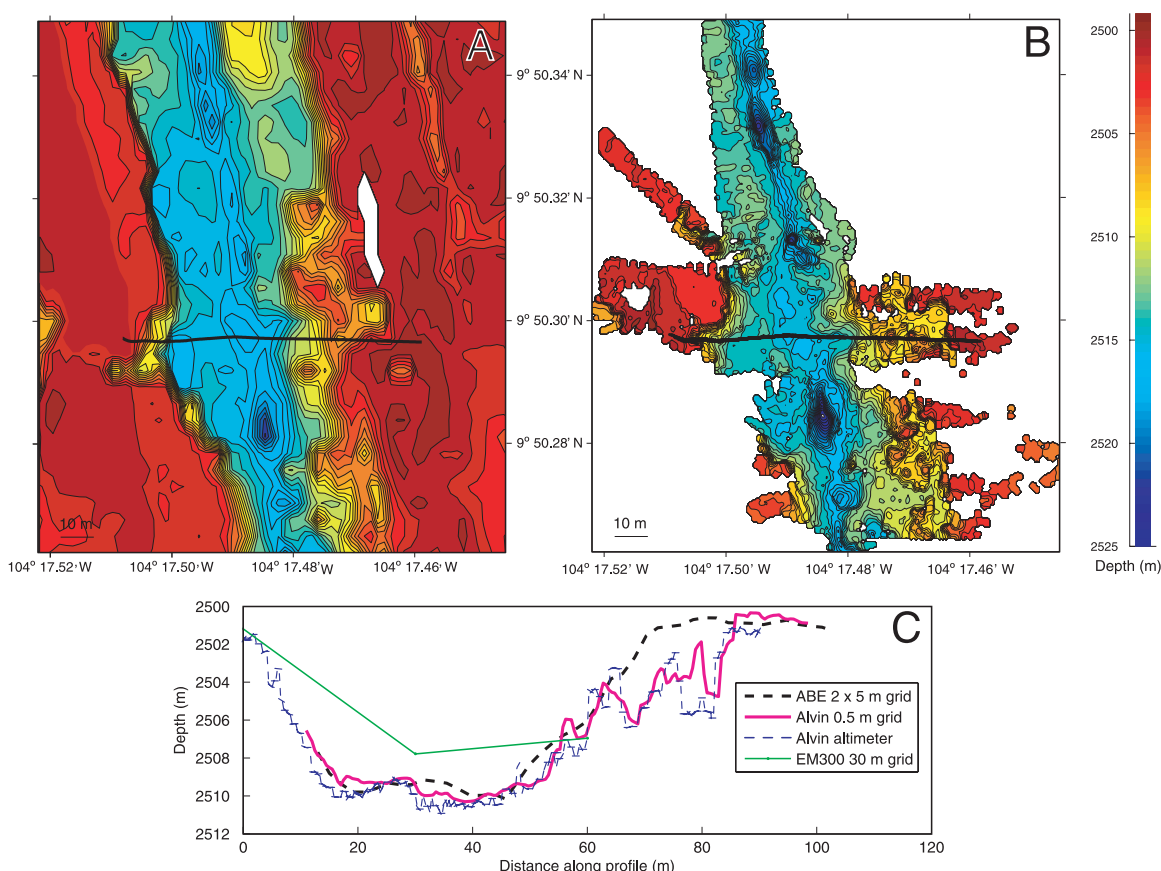
Figure 11. Comparison of bathymetric resolution achieved with ABE and *Alvin* mapping strategies. (a) ABE 2 m (east–west) × 5 m (north–south) grid with 0.5-m contours generated with previously reported data [*Fornari et al.*, 2004]. This map reveals much of the complexity of the axial trough at the EPR surrounding Bio1 and Bio9 and P vent sites. (b) *Alvin* 0.5-m composite grid (0.5-m contours) for the same areas as Figure 11a, revealing many of the features identified in Figure 11a but at higher resolution. The consistency of these maps indicates the success of the grid rectification technique. Differences in resolution between the composite grid (Figure 11b) and the 2 m × 5 m ABE grid (Figure 11a) are primarily related to the increased data density and smaller acoustic footprint size associated with the low-altitude *Alvin* surveys. (c) Comparison of ABE 2 × 5 m grid, *Alvin* 0.5-m grid, *Alvin* altimeter profile, and EM300 30-m grid [*White et al.*, 2006]. Profiles are from west to east (looking north), and their location is indicated in Figures 11a and 11b. Note that the ABE data were vertically shifted by 2 m to be broadly consistent with the *Alvin* data.

AST floor, but the diffuse flow biological communities extend across the entire width of AST (Figures 10a and 10b).

4. Discussion

4.1. Comparisons of *Alvin* Composite Grids With ABE Maps

[42] ABE bathymetry data provide important geologic context for the small composite maps presented here. In addition, comparing the ABE maps (2 m × 5 m grid) with *Alvin* composite grids (0.5 m grid) (e.g., Figures 11 and 12) ensures that the composite grids are realistic and accurate. Bathy-

metric features that are evident in the ABE data (Figure 11a) are generally better resolved in the *Alvin* composite grids (Figure 11b) because of increased data density, and the smaller acoustic footprint size associated with low-altitude *Alvin* surveys (Figure 2). The greater coverage afforded by the ABE data, however, provides important spatial context for understanding the along-strike continuity and for constraining the location of the AST walls. The elongation of bathymetric contours in the north-south (along-track) direction in the ABE grid (Figure 11a) compared with the *Alvin* composite grid is primarily due lower data density in the along-track (north–south) direction. In ad-
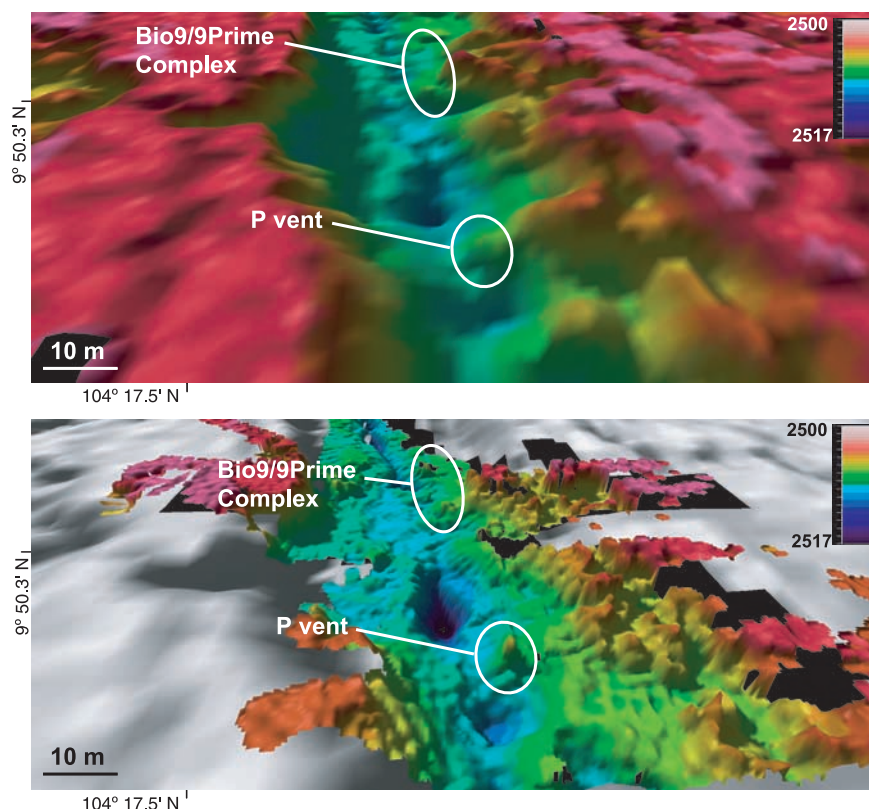
Figure 12. Three-dimensional visualization (1X vertical exaggeration) of (top) the ABE 2 × 5 m grid and (bottom) *Alvin* 0.5 m composite grid embedded within ABE grid. The finer-scale (0.5-m grid) *Alvin* grid clearly shows the extensively collapsed and irregular morphology of the AST wall attributed primarily to localized eruption focusing, drainback and collapse [e.g., *Fornari et al.*, 1998a, 2004]. Note that the ability to identify hydrothermal structures and to interpret the fine-scale morphology of the eastern AST wall is heavily dependent on the resolution of the bathymetry data.

dition, the bathymetric features themselves are elongate in the north–south direction (Figure 11).

[43] One of the significant benefits of the larger ABE grid is that it covers a wide area across the EPR summit plateau, and the distribution of lava channels and lava flow fronts can therefore be accurately determined and correlated with features mapped using side scan sonar [*Schouten et al.*, 2002; *Fornari et al.*, 2004; *Soule et al.*, 2005]. The ABE data also provide the topographic context for properly processing and interpreting the near-bottom magnetic data collected during the ABE surveys which resolve the character of the central anomaly magnetic high (CAMH) [*Schouten et al.*, 1999, 2002] and distribution of highly magnetic flows associated with recent volcanism over the past ~80 ka. These data sets are important to understanding the development of young ocean crust and shallow crustal structure at this fast spreading MOR [e.g., *Bowles et al.*, 2006; *Tivey et al.*, 2003; A. Tivey et al., manuscript in prepa-

ration, 2006]. Although the larger-scale bathymetric maps that exist for this site [e.g., *Schouten et al.*, 2002; *Fornari et al.*, 2004] provide a useful and important synoptic perspective, the spatially limited but higher-resolution *Alvin* grids provide additional information that can be used to better understand the complex interplay of volcanic, tectonic, and hydrothermal processes at the ridge axis.

[44] The detailed morphologic features resolved in the composite grids of the AST have important implications for deducing the volcanic history and relationships between volcanic and hydrothermal processes [e.g., *Fornari et al.*, 2004]. The limited illumination from *Alvin*, extending only ~5–10 m from the vehicle, and the chaotic nature of the lava flows, primary eruptive fissure(s), and extensive lava pillars along the AST wall throughout the study area, have made it difficult to get a broad overview of the morphology of the terrain from visual observations. The submeter grids shown

here provide the quantitative context for under-standing possible causal relationships between geologic features such as lava channels and break-outs in the AST wall and hydrothermal vents within AST [*Fornari et al.*, 2004].

[45] Three key geological features present in the AST are well resolved by the new submeter bathymetry: (1) the primary fissure, (2) lava pillars and groups of pillars forming ramparts along the AST floor and wall, and (3) the severely embayed margins/walls of the trough. The improved resolu-tion of these features is evident in all the composite grids, but perhaps most obvious in Figure 11 where the contrast between the ABE and *Alvin* data shows the benefits of the lower altitude surveys and finer grid resolution. The morphologic character of the primary fissure shown in Figures 6−8 and 10−11 is variable along the AST between 9°49′ and 50′N. It can be as narrow as ~1 m and several meters deep to nearly 10 m wide and >5−7 m deep. The variable continuity of the fissure, as imaged in the bathymetry suggests that during the 1991 event, the eruption focused in places possibly creating the deep holes. In some cases a shallow fissure seg-ment connects the holes suggesting posteruption drainback may have contributed to infilling along portions of the fissure.

[46] Lava pillars can easily be identified from *Alvin's* view ports, but their bathymetric character and the spatial relationships between groups of pillars and how they create the AST wall have never been resolved until production of the com-posite grids presented here. Figure 6b clearly shows the abundance of small, 1- to 2-m-diameter pillars, as well as larger coalesced pillar ramparts that are frequently associated with the eastern AST wall in the 9°50.3′N area. The abundance of pillars in this area suggests that fluid flow along the margin of the AST prior to the eruption was robust and that as the 1991 flow was erupting lava pillar formation was accentuated in this area. There is a marked contrast between the western margin of the AST in this area that has few pillars, and the eastern wall that is replete with them. The relative abundance of pillars within the AST, and linea-tions formed by groups of pillars can be used to deduce preeruption fluid egress sites. The spatial relationships between pillars and hydrothermal chimneys can now be better resolved with the composite maps and in some cases causal relation-ships can be suggested. An example of this is the observation that during the 1991 eruption, some

hydrothermal venting occurred from the top of lava pillars [*Haymon et al.*, 1993].

[47] The increasingly high resolution of near-bottom sonar surveys, and the fact that these data are often 10−100 times better than previously available surface ship multibeam, brings into ques-tion the extent to which greater resolution bathy-metric maps are needed for various seafloor study areas. Simply put, marine geologists require the same high-resolution "topographic" information as terrestrial geologists in order to properly deduce terrain morphology and its causal relationship to geological and other seafloor processes. Digital elevation models (DEMs) of land-based study sites are now commonplace and play an important role in visualizing field areas, locating important features, and ascribing process-oriented relation-ships to prominent features. Until recently, this sort of detailed information was not available to marine geologists studying deep-water environments (e.g., Figure 11c). With continued advances in technol-ogy, and the creation of high-resolution maps of the seafloor, we can now begin to identify the spatial signatures of the processes that shape the seafloor, and we can better understand the dynam-ics and interactions between complex biological-hydrothermal-geological processes.

[48] While the high-resolution mapping techniques we employ can resolve the spatial dimensions and relationships of seafloor features, this technique is limited in its ability to map biological communities and animal aggregations. Currently, photographic image data is required to construct noninvasive community-scale maps and assess the distribution and composition of endemic faunal communities over local scales. By combining high-resolution photographic imaging surveys and simultaneous near-bottom high-resolution bathymetric mapping, the systematic spatial distribution of seafloor fea-tures (and ultimately temporal processes that create them) can be correlated with the distribution and composition of biological communities and used to suggest causal linkages among them. For example, the associative relationships of distinct and similar invertebrate communities in diffuse flow habitats, including fissure margins, collapse pits, and lava pillar tops can be identified, and the causal pro-cesses structuring the distribution of venting and composition of biological communities can be investigated.

[49] Future improvements in microbathymetric mapping resolution to the centimeter scale may be realized using laser line scanning over limited

areas. Increased navigational accuracy over small areas, afforded by high-frequency, ultra short-baseline transponder arrays in conjunction with construction of centimeter-scale photomosaics that represent a time series of data will provide the mapping accuracy and the biologically relevant and necessary scale to examine the processes responsible for temporal changes in faunal community structure. These include faunal colonization in specific physical and chemical microhabitats, successional shifts in dominant fauna over time and with changes in vent fluid chemistry, and community demise due to lava collapse, fissure infilling, sulfide chimney collapse, and other temporal changes in geological features including resets in the hydrothermal and biological cycles induced by volcanic eruptions.

4.2. Grid Rectification

[50] The grid rectification algorithm used to generate composite grids is an important step toward routinely utilizing *Alvin* dive time for bathymetric surveys, and provides a framework for continued detailed mapping with *Alvin*. There are two ways in which this tool can be used in the future: (1) existing composite grids can be augmented by including additional data collected during repeat *Alvin* dives at the same site and (2) composite grids can be generated to create a time series of bathymetric data that can be used to quantify changes associated with hydrothermal systems and volcanic/tectonic processes at the ridge axis.

[51] The grid rectification algorithm is a final processing step that can be used to address positioning offsets that remain after navigational data are fully postprocessed. It can be used to combine any sparse spatially gridded data into a composite map as long as there is sufficient overlap between data sets to identify at least five GCPs. It is ideal for use with the Imagenex 881 data routinely collected with *Alvin* because it permits the ingestion of data even if the data are not collected during planned bathymetric surveys. This technique assumes that each gridded data set being incorporated into the composite map is internally consistent, and it allows for small displacements of bathymetric data points based features resolved in individual grids. Errors in the composite grids can be easily identified (see Figure 6b) by utilizing the error estimator presented by *Roman and Singh* [2006], and data can be limited to areas where the error is below a user-defined threshold.

[52] Small navigational offsets inherent to underwater vehicle navigation can also be overcome with the use of a Simultaneous Localization and Mapping (SLAM) technique [*Roman*, 2005; *Roman and Singh*, 2005]. This technique divides a survey into a series of overlapping submaps, which are iteratively registered to one another using a Kalman filter. It is particularly useful for ensuring that data collected in a single survey are self-consistent and is applicable to scanning sonar data collection provided that the data are sufficiently dense and have sufficient overlap between adjacent survey lines. As a result, it works best with near-bottom multibeam data obtained during dedicated comprehensive surveying efforts, as demonstrated by *Roman and Singh* [2005] and *Roman et al.* [2005]. However, in its current configuration, this algorithm is incapable of automatically merging data from multiple dives into a single composite map, so the issue of where the final map product resides in geographic space depends on the accuracy of vehicle's navigational systems, and the use of grid rectification techniques.

5. Conclusions and Suggestions for Future Directions

[53] Although it is not efficient to utilize *Alvin* as a primary platform for surveying tens of square kilometers of seafloor, it is reasonable to acquire near-bottom scanning or multibeam sonar data during all dive operations and to dedicate small periods of time to high-resolution mapping, particularly if dive time remains after the primary objectives have been met. Since *Alvin* revisits many of the same sites frequently, the grid rectification technique provides a means for building composite maps over small areas and for quantifying bathymetric change. The efficiency of near bottom surveying efforts conducted with *Alvin*, and the resolution of the resulting map products, would increase significantly if the Imagenex scanning sonar were replaced with a high-frequency multibeam sonar system, as is the case with both ABE and Jason 2.

[54] High-precision navigational data is a critical component for high-resolution mapping efforts. It also improves the accuracy of sample positioning within the context of high-resolution maps, and provides a baseline for time series observations. The resolution of near-bottom high-frequency sonar data sets will continue to improve in the future, particularly as navigational precision and

accuracy improve. In the meantime, careful attention is required during field operations to ensure the highest quality navigational data acquisition. This can be facilitated by the use of permanent seafloor benchmarks that can be visited for brief periods during each dive to help constrain navigational uncertainties.

[55] Composite maps can be compiled by coordinating efforts between field programs and designing surveys based upon existing high-resolution bathymetry data. This was the case in 2004–2005 when biologists and geologists working at the EPR collaborated in collecting the data presented here. Utilizing currently available software tools to process vehicle navigation between dives will facilitate survey planning and optimize continued surveying efforts.

[56] High-resolution (submeter) composite maps generated from multiple dives can be compiled and nested within existing maps (e.g., 2 × 5 m ABE grid, 5 m ABE grid, and 25–100 m multibeam). Combining these data sets permits the quantification of submeter bathymetric features including hydrothermal vent structures, lava pillars, and small fissures and faults within the context of larger-scale bathymetric and structural patterns. In addition, nested data sets provide a means of quality controlling newly generated composite maps.

6. Postscript

[57] During the revision of this paper, a recent eruption was confirmed at the EPR ISS through data acquisition on several rapid response cruises. The initial evidence for an eruption came from nonrecovery of eight ocean bottom seismometers (OBSs) deployed as part of the microseismic monitoring program at the ISS [*Weekly et al.*, 2005]. That evidence led scientists doing the OBS recovery to conduct bottom water properties surveys using a MAPR [*Baker et al.*, 2004] and to dredge the EPR axis near 9°48′N. Extensive evidence for potential temperature and turbidity anomalies in the near-bottom water suggested that the hydrothermal state of the EPR axis in the area had changed, possibly due to a recent eruption. Two "response" cruises followed. The R/V *New Horizon* cruise in May 2006 (06 NH) acquired detailed CTD tow-yo and TowCam photographic data [*Fornari and the WHOI TowCam Group*, 2003] and unequivocally documented that an eruption had occurred [*Cowen et al.*, 2006]. The second

cruise was carried out on the R/V *Atlantis* (AT15-6) in June 2006, utilizing *Alvin* and a fiber optic towed camera system to survey and sample the area. Preliminary findings from these cruises are reported by *Tolstoy et al.* [2006], *Cowen et al.* [2006] and at the Ridge2000 website (http://www.ridge2000.org/). The submeter maps produced as part of the work we report on here now provide the relevant bathymetric baseline data to unequivocally determine the magnitude and spatial limits of changes that have occurred in the AST as a result of the 2005–2006 eruption(s). Some evidence for these changes derived from the Imagenex data acquired on the June 2006 *Alvin* dives suggests that the AST in places is narrower and deeper than previously mapped [*Ferrini et al.*, 2006]. Subsequent acquisition of Imagenex 881 data using *Alvin* on dives planned for 2006–2007 will provide fundamental insights into the formation of local seafloor features. Repeat mapping of the AST over the eruption area between 9°46′–55′N region using near-bottom multibeam would be the most effective means for providing key data on (1) how the AST has changed; (2) how changes relate to the locations of new and old hydrothermal vents and biological communities; and (3) to reestablish the physical baseline of the axial morphology.

Acknowledgments

References

Agnew, D. C. (1996), SPOTL: Some Programs for Ocean-Tide Loading, *SIO Ref. Ser.*, *96–8*, 34 pp.

Bachmayer, R., et al. (1998), Oceanographic research using remotely operated underwater robotic vehicles: exploration of hydrothermal vent sites on the Mid-Atlantic Ridge at 37°N 32°W, *Mar. Technol. Soc. J.*, *32*(3), 37–47.

Baker, E. T., R. P. Lowell, J. A. Resing, R. A. Feely, R. W. Embley, G. J. Massoth, and S. L. Walker (2004), Decay of hydrothermal output following the 1998 seafloor eruption at Axial Volcano: Observations and models, *J. Geophys. Res.*, *109*, B01205, doi:10.1029/2003JB002618.

Ballard, R. D., et al. (2000), The discovery of ancient history in the deep sea using advanced deep submergence technology, *Deep Sea Res., Ser. I*, *47*(9), 1591–1620.

Bowles, J., J. S. Gee, D. V. Kent, M. R. Perfit, S. A. Soule, and D. J. Fornari (2006), Paleointensity applications to timing and extent of eruptive activity, 9°–10°N East Pacific Rise, *Geochem. Geophys. Geosyst.*, *7*, Q06006, doi:10.1029/2005GC001141.

Chadwick, W. W., Jr. (2003), Quantitative constraints on the growth of submarine lava pillars from a monitoring instrument that was caught in a lava flow, *J. Geophys. Res.*, *108*(B11), 2534, doi:10.1029/2003JB002422.

Chadwick, W. W., Jr., D. S. Scheirer, R. W. Embley, and H. P. Johnson (2001), High-resolution bathymetric surveys using scanning sonars: Lava flow morphology, hydrothermal vent and geologic structure at recent eruption sites on the Juan de Fuca Ridge, *J. Geophys. Res.*, *106*, 16,075–16,100.

Cochran, J. R., D. J. Fornari, B. J. Coakley, R. Herr, and M. A. Tivey (1999), Continuous near-bottom gravity measurements made with a BGM-3 gravimeter in DSV *Alvin* on the East Pacific Rise crest near 9°30′N and 9°50′N, *J. Geophys. Res.*, *104*, 10,841–10,861.

Cormier, M. H., W. B. F. Ryan, A. Shah, W. Jin, A. M. Bradley, and D. R. Yoerger (2003), Waxing and waning volcanism along the East Pacific Rise on a millennium timescale, *Geology*, *31*, 633–636.

Cowen, J. P., et al. (2006), Volcanic eruptions at East Pacific Rise Near 9°50′N, *Eos Trans. AGU*, in press.

de Moustier, C. (1988), State of the art in swath bathymetry survey systems, *Int. Hydrogr. Rev.*, *65*(2), 25–54.

Detrick, R. S., P. Buhl, E. Vera, J. Mutter, J. Orcutt, J. Madsen, and T. Brocher (1987), Multichannel seismic imaging of a crustal magma chamber along the East Pacific Rise between 9°N and 13°N, *Nature*, *326*, 35–41.

Dunn, R. A., and D. R. Toomey (1997), Seismological evidence for three-dimensional melt migration beneath the East Pacific Rise, *Nature*, *388*, 259–262.

Embley, R. W. (2002), Rediscovery and exploration of Magic Mountain, Explorer Ridge, NE Pacific, *Eos Trans. AGU*, *83*(47), Fall Meet. Suppl., Abstract T11C-1264.

Engels, J. L., M. H. Edwards, D. J. Fornari, M. R. Perfit, and J. R. Cann (2003), A new model for submarine volcanic collapse formation, *Geochem. Geophys. Geosyst.*, *4*(9), 1077, doi:10.1029/2002GC000483.

Ferrini, V., D. J. Fornari, T. Shank, M. Tivey, D. S. Kelley, D. Glickson, S. M. Carbotte, J. Howland, L. L. Whitcomb, and D. Yoerger (2004), Very high resolution bathymetric mapping at the Ridge 2000 integrated study sites: Acquisition and processing protocols developed during recent *Alvin* field programs to the East Pacific Rise and Juan de Fuca Ridge, *Eos Trans. AGU*, *85*(47), Fall Meet. Suppl., Abstract B13A-0162.

Ferrini, V. L., L. Whitcomb, J. Howland, D. Fornari, S. M. Carbotte, D. Kelley, T. Shank, and M. Tivey (2005a), Navigation of UNOLS National Deep Submergence Facility (NDSF) vehicles: Status report and guidelines for data

acquisition, paper presented at Ridge 2000 Community Progress and Planning Workshop, Natl. Sci. Found., Vancouver, B. C., Canada.

Ferrini, V., A. Sterling, F. Martinez, M. K. Tivey, M. Mottl, and S. Kim (2005b), High-resolution micro-bathymetry mapping in the Lau Basin: Examples from the Tu'i Malila and Mariner vent sites, *Eos Trans. AGU*, *86*(52), Fall Meet. Suppl., Abstract T31A-0476.

Ferrini, V. L., S. A. Soule, D. J. Fornari, K. L. Von Damm, T. Shank, M. R. Perfit, and K. H. Rubin (2006), Small-scale bathymetric changes associated with 2005–2006 eruptions at the East Pacific Rise near 9°50′N, *Eos Trans. AGU*, *87*(52), Fall Meet. Suppl., Abstract V23B-0604.

Fornari, D. J., and R. W. Embley (1995), Tectonic and volcanic controls on hydrothermal processes at the mid-ocean ridge: An overview based on near-bottom and submersible studies, in *Physical, Chemical, Biological, and Geological Interactions within Seafloor Hydrothermal Systems*, *Geophys. Monogr. Ser.*, vol. 91, edited by S. E. Humphris et al., pp. 1–46, AGU, Washington, D. C.

Fornari, D. J., and the WHOI TowCam Group (2003), A new deep-sea towed digital camera and multi-rock coring system, *Eos Trans. AGU*, *84*(8), 69.

Fornari, D. J., M. R. Perfit, J. F. Allan, R. Batiza, R. Haymon, A. Barone, W. B. F. Ryan, T. Smith, T. Simkin, and M. A. Luckman (1988), Geochemical and structural studies of the Lamont Seamount—Seamounts as indicators of mantle processes, *Earth Planet. Sci. Lett.*, *89*(1), 63–83.

Fornari, D. J., R. M. Haymon, M. R. Perfit, T. K. P. Gregg, and M. H. Edwards (1998a), Geological characteristics and evolution of the Axial Zone on fast spreading mid-ocean ridges: Formation of an axial summit trough along the East Pacific Rise, 9°–10°N, *J. Geophys. Res.*, *103*, 9827–9855.

Fornari, D. J., T. Shank, K. L. Von Damm, T. K. P. Gregg, M. Lilley, G. Levai, A. Bray, R. M. Haymon, M. R. Perfit, and R. Lutz (1998b), Time-series temperature measurements at high-temperature hydrothermal vents, East Pacific Rise 9° 49′–51′N: Monitoring a crustal cracking event, *Earth Planet. Sci. Lett.*, *160*, 419–431.

Fornari, D. J., et al. (2004), Submarine lava flow emplacement at the East Pacific Rise 9°50′N: Implications for uppermost ocean crust stratigraphy and hydrothermal fluid circulation, in *Mid-Ocean Ridges: Hydrothermal Interactions Between the Lithosphere and Oceans*, *Geophys. Monogr. Ser.*, vol. 148, edited by C. R. German, J. Lin, and L. M. Parson, pp. 187–218, AGU, Washington, D. C.

Gregg, T. K. P., D. J. Fornari, M. R. Perfit, R. M. Haymon, and J. H. Fink (1996), Rapid emplacement of a mid-ocean ridge lava flow: The East Pacific Rise at 9°46′–51′N, *Earth Planet. Sci. Lett.*, *144*, E1–E7.

Harding, A. J., G. M. Kent, and J. A. Orcutt (1993), A multi-channel seismic investigation of upper crustal structure at 9°N on the East Pacific Rise: Implications for crustal accretion, *J. Geophys. Res.*, *98*, 925–13,944.

Haymon, R. M., D. J. Fornari, M. H. Edwards, S. Carbotte, D. Wright, and K. C. Macdonald (1991), Hydrothermal vent distribution along the East Pacific Rise crest (9°09′–54′N) and its relationship to magmatic and tectonic processes on fast-spreading mid-ocean ridges, *Earth Planet. Sci. Lett.*, *104*, 513–534.

Haymon, R. M., D. J. Fornari, K. L. Von Damm, M. D. Lilley, M. R. Perfit, and J. M. Edmond (1993), Volcanic eruption of the mid-ocean ridge along the East Pacific Rise crest at 9°45′–52′N: Direct submersible observations of seafloor phenomena associated with an eruption event in April, 1991, *Earth Planet. Sci. Lett.*, *119*, 85–101.

Hey, R., et al. (2004), Tectonic/volcanic segmentation and controls on hydrothermal venting along Earth's fastest seafloor spreading system, EPR 27°–32°S, *Geochem. Geophys. Geosyst.*, *5*, Q12007, doi:10.1029/2004GC000764.

Hunt, M. M., W. M. Marquet, D. A. Moller, K. R. Peal, W. K. Smith, and R. C. Spindell (1974), An acoustic navigation system, *WHOI Tech. Rep. WHOI-74-6,* Woods Hole Oceanogr. Inst., Woods Hole, Mass.

Jakuba, M., D. Yoerger, W. Chadwick, A. Bradley, and R. Embley (2002), Multibeam sonar mapping of the Explorer Ridge with an autonomous underwater vehicle, *Eos Trans. AGU, 83*(47), Fall Meet. Suppl., Abstract T11C-1266.

Johnson, H. P., et al. (2002), Survey studies hydrothermal circulation on the northern Juan de Fuca Ridge, *Eos Trans. AGU*, *83*, 73.

Kelley, D. S., et al. (2005), A serpentinite-hosted ecosystem: The Lost City Hydrothermal Field, *Science*, *307*, 1428–1434.

Kent, G. M., J. C. Mutter, P. Buhl, A. J. Harding, J. A. Orcutt, and R. S. Detrick (1994), Uniform accretion of oceanic crust south of the Garrett transform at 14°15′S on the East Pacific Rise, *J. Geophys. Res.*, *99*, 9097–9116.

Kinsey, J. C., and L. L. Whitcomb (2002), Towards in-situ calibration of Gyro and Doppler Navigation sensors for precision underwater vehicle navigation, paper presented at the 2002 IEEE International Conference on Robotics and Automation, Arlington, Va.

Kinsey, J. C., and L. L. Whitcomb (2004), Preliminary field experience with the DVLNAV integrated navigation system for oceanographic submersibles, *Control Eng. Pract.*, *12*, 1541–1549.

Kinsey, J. C., and L. L. Whitcomb (2006), In-situ alignment calibration of attitude and Doppler sensors for precision underwater vehicle navigation: Theory and experiment, *IEEE J. Oceanic Eng.*, in press.

Kurras, G. J., M. H. Edwards, and D. J. Fornari (1998), High-resolution bathymetry of the East Pacific Rise axial summit trough 9°49′–51′N: A compilation of *Alvin* scanning sonar and altimetry data from 1991–1995, *Geophys. Res. Lett.*, *25*(8), 1209–1212.

Kurras, G., D. J. Fornari, and M. H. Edwards (2000), Volcanic morphology of the East Pacific Rise crest 9°49′–52′N: Implications for extrusion at fast spreading mid-ocean ridges, *Mar. Geophys. Res.*, *21*, 23–41.

Lutz, R. A., T. M. Shank, D. J. Fornari, R. M. Haymon, M. D. Lilley, K. L. Von Damm, and D. Desbruyeres (1994), Rapid growth at deep-sea vents, *Nature*, *371*, 663–664.

Lutz, R. A., C. Vetriani, G. W. Luther, T. M. Shank, and M. Tolstoy (2005), Integrated studies of biological community structure at deep-sea hydrothermal vents: A project overview, paper presented at Ridge 2000 Community Progress and Planning Workshop, Natl. Sci. Found., Vancouver, B. C., Canada.

Macdonald, K. C., J.-C. Sempere, and P. J. Fox (1984), East Pacific Rise from Siqueiros to Orozco fracture zones: Along-strike continuity of axial neovolcanic zone and structure and evolution of overlapping spreading centers, *J. Geophys. Res.*, *89*, 6049–6069.

Macdonald, K. C., et al. (1992), The East Pacific Rise and its flanks 8°–18°N: History of segmentation, propagation and spreading direction based on SeaMARC II and SeaBeam studies, *Mar. Geophys. Res.*, *14*, 299–344.

Milne, P. H. (1983), *Underwater Acoustic Positioning Systems*. Gulf Publ., Houston, Tex.

Moore, T. S., T. J. Waite, B. T. Glazer, D. M. Nuzzio, T. M. Shank, and G. W. Luther (2005), Time-series electrochemi-cal analysis from the 9°N EPR vents sites, paper presented at Ridge 2000 Community Progress and Planning Workshop, Natl. Sci. Found., Vancouver, B. C., Canada.

Roman, C. (2005), Self consistent bathymetric mapping from robotic vehicles in the deep ocean, Ph.D. dissertation, 129 pp., Mass. Inst. of Technol., Cambridge.

Roman, C., and H. Singh (2005), Improved vehicle based multibeam bathymetry using sub-mapping and SLAM, paper presented at the 2005 IEEE International Conference on Intelligent Robots and Systems (IROS), Edmonton, Alberta, Canada.

Roman, C., and H. Singh (2006), Consistency based error evaluation for deep sea bathymetric mapping with robotic vehicles, paper presented at the 2006 IEEE International Conference on Robotics and Automation, Orlando, Fla.

Roman, C., R. Reves-Sohn, H. Singh, and S. Humphris (2005), Self consistent bathymetric mapping using sub-maps: Survey results from the TAG hydrothermal structure, *Eos Trans. AGU*, *86*(52), Fall Meet. Suppl., Abstract OS33A-1465.

Rubin, K. H., J. D. MacDougall, and M. R. Perfit (1994), ^{210}Po/^{210}Pb dating of recent volcanic eruptions on the sea floor, *Nature*, *468*, 841–844.

Scheirer, D. S., D. J. Fornari, S. E. Humphris, and S. Lerner (2000), High-resolution seafloor mapping using the DSL-120 sonar system: Quantitative assessment of sidescan and phase-bathymetry data from the Lucky Strike Segment of the Mid-Atlantic Ridge, *Mar. Geophys. Res.*, *21*, 121–142.

Scheirer, D. S., T. M. Shank, and D. J. Fornari (2006), Temperature variations at diffuse and focused flow hydrothermal vent sites along the northern East Pacific Rise, *Geochem. Geophys. Geosyst.*, *7*, Q03002, doi:10.1029/2005GC001094.

Schouten, H., M. A. Tivey, D. J. Fornari, and J. R. Cochran (1999), Central Anomaly Magnetization High: Constraints on the volcanic construction and architecture of seismic layer 2A at a fast-spreading mid-ocean ridge, the EPR at 9°30′–50′N, *Earth Planet. Sci. Lett.*, *169*, 37–50.

Schouten, H., M. Tivey, D. Fornari, D. Yoerger, A. Bradley, P. Johnson, M. Edwards, and T. Kurokawa (2002), Lava transport and accumulation processes on EPR 9 27′N to 10N: Interpretations based on recent near-bottom sonar imaging and seafloor observations using ABE, *Alvin* and a new digital deep sea camera, *Eos Trans. AGU*, *83*(47), Fall Meet. Suppl., Abstract T11C-1262.

Shank, T. M., D. J. Fornari, K. L. Von Damm, M. D. Lilley, R. M. Haymon, and R. A. Lutz (1998), Temporal and spatial patterns of biological community development at nascent deep-sea hydrothermal vents along the East Pacific Rise, *Deep Sea Res., Part II*, *45*, 465–515.

Shank, T. M., et al. (2003), Deep submergence synergy: *Alvin* and ABE explore the Galápagos Rift at 86°W, *Eos Trans. AGU*, *84*(41), 425.

Shank, T. M., S. Beaulieu, G. Luther, W. Seyfried, K. Ding, V. Vetriani, S. Sievert, and R. A. Lutz (2005), Integrative approaches to understanding the interaction of fluid chemistry and microbial biofilms on larval settlement on the East Pacific Rise, paper presented at Ridge 2000 Community Progress and Planning Workshop, Natl. Sci. Found., Vancouver, B. C., Canada.

Singh, H., L. Whitcomb, D. Yoerger, and O. Pizarro (2000), Microbathymetric Mapping from Underwater Vehicles in the Deep Ocean, *Comp. Vision Image Understanding*, *79*, 143–161.

Sinton, J., E. Bergmanis, K. Rubin, R. Batiza, T. K. P. Gregg, K. Grönvold, K. C. Macdonald, and S. M. White (2002), Volcanic eruptions on mid-ocean ridges: New evidence from

the superfast spreading East Pacific Rise, 17°–19°S, *J. Geo-phys. Res.*, *107*(B6), 2115, doi:10.1029/2000JB000090.

Soule, S. A., D. J. Fornari, M. R. Perfit, M. A. Tivey, W. I. Ridley, and H. Schouten (2005), Channelized lava flows at the East Pacific Rise crest 9°–10°N: The importance of off-axis lava transport in developing the architecture of young oceanic crust, *Geochem. Geophys. Geosyst.*, *6*, Q08005, doi:10.1029/2005GC000912.

Tivey, M. A., A. Bradley, D. Yoerger, R. Catanach, A. Duester, S. Liberatore, and H. Singh (1997), Autonomous underwater vehicle maps seafloor, *Eos Trans. AGU*, *78*, 229.

Tivey, M. A., H. P. Johnson, A. Bradley, and D. Yoerger (1998), Thickness measurements of submarine lava flows determined from near-bottom magnetic field mapping by autonomous underwater vehicle, *Geophys. Res. Lett.*, *25*, 805–808.

Tivey, M. A., D. Fornari, H. Schouten, A. Bradley, D. Yoerger, H. P. Johnson, R. Embley, W. Chadwick, T. Shank, and S. Hammond (2003), High-resolution magnetic field and bathymetric imaging using autonomous underwater vehicles, remotely operated vehicles and submersibles, *EGS-AGU-EUG Spring Meeting*, *5*, 2858, Abstract EAE03-A02858.

Tolstoy, M., et al. (2006), A seafloor spreading event captured by seismometers, *Science*, doi:10.1126/science.1133950.

Toomey, D. R., S. C. Solomon, and G. M. Purdy (1994), Tomographic imaging of the shallow crustal structure of the East Pacific Rise at 9°30′N, *J. Geophys. Res.*, *99*, 24,135–24,157.

Von Damm, K. L. (2000), Chemistry of hydrothermal vent fluids from 9–10°N, East Pacific Rise: "Time zero" the immediate post-eruptive period, *J. Geophys. Res.*, *105*, 11,203–11,222.

Von Damm, K. L., A. M. Bray, L. G. Buttermore, M. D. Lilley, E. J. Olson, and E. McLaughlin (1996), Chemical changes between high temperature and diffuse flow fluids at 9°50′N East Pacific Rise, *Eos Trans. AGU*, *77*(46), Fall Meet. Suppl., F403–404.

Von Damm, K. L., and M. D. Lilley (2004), Diffuse flow hydrothermal fluids from 9°50′N East Pacific Rise: Origin, evolution, and biogeochemical controls, in *The Subsurface Biosphere at Mid-Ocean Ridges*, *Geophys. Monogr. Ser.*, vol. 144, edited by W. S. D. Wilcock et al., pp. 245–268, AGU, Washington, D. C.

Weekly, R. T., M. Tolstoy, F. Waldhauser, D. R. Bohnenstiehl, and W. Kim (2005), Increasing seismic activity at 9deg50′N on the East Pacific Rise RIDGE 2000 integrated studies site from October 2003 through April 2004, *Eos Trans. AGU*, *86*(52), Fall Meet. Suppl., Abstract T31A-0495.

Whitcomb, L. L., D. R. Yoerger, H. Singh, and D. A. Mindell (1998), Towards precision robotic maneuvering, survey, and manipulation in unstructured undersea environments, in *Robotics Research: The Eighth International Symposium*, edited by Y. Shirai and S. Hirose, pp. 45–54, Springer, New York.

Whitcomb, L., D. R. Yoerger, and H. Singh (1999a), Combined Doppler/LBL based navigation of underwater vehicles, paper presented at the 11th International Symposium on Unmanned Untethered Submersible Technology, Autonomous Undersea Syst. Inst., Durham, N. H.

Whitcomb, L. L., D. R. Yoerger, and H. Singh (1999b), Advances in Doppler-based navigation of underwater robotic vehicles, paper presented at the IEEE International Conference on Robotics and Automation, Detroit, Mich.

Whitcomb, L. L., D. R. Yoerger, H. Singh, and J. Howland (2000), Advances in underwater robot vehicles for deep ocean exploration: Navigation, control, and survey operations, in *Robotics Researc:- The Ninth International Symposium*, pp. 439–448, Springer, New York.

Whitcomb, L., J. Kinsey, D. Yoerger, C. Taylor, A. Bowen, B. Walden, and D. Fornari (2003), Navigation upgrades to the National Deep Submergence Facility vehicles D. S. V. *Alvin*, Jason 2, and the DSL-120A, *Eos Trans. AGU*, *84*(46), Fall Meet. Suppl., Abstract OS32A-0225.

White, S. M., R. Haymon, and S. M. Carbotte (2006), A new view of ridge segmentation and near-axis volcanism at the East Pacific Rise, 8°–12°N, from EM300 multibeam bathymetry, *Geochem. Geophys. Geosyst.*, *7*, Q12O05, doi:10.1029/2006GC001407.

Yoerger, D., A. Bradley, R. Bachmayer, R. Catanach, A. Duester, S. Liberatore, H. Singh, B. Walden, and M. A. Tivey (1996), Near-bottom magnetic surveys of the Coaxial Ridge segment using the Autonomous Benthic Explorer survey vehicle, *RIDGE Events*, *7*, 5–9.

Yoerger, D. R., A. M. Bradley, B. B. Walden, H. Singh, and R. Bachmayer (1998), Surveying a subsea lava flow using the Autonomous Benthic Explorer (ABE), *Int. J. Syst. Sci.*, *10*(29), 1031–1044.

Yoerger, D. R., A. M. Bradley, B. B. Walden, M.-H. Cormier, and W. B. F. Ryan (2000), Fine-scale seafloor survey in rugged deep-ocean terrain with an autonomous robot, paper presented at the 2000 IEEE International Conference on Robotics and Automation, San Francisco, Calif.

Yoerger, D. R., R. Collier, and A. M. Bradley (2002), Hydrothermal vent plume discovery and survey with an autonomous underwater vehicle, *Eos Trans. AGU*, *83*(47), Fall Meet. Suppl., Abstract T11C-1261.